⊛**MSNW**

SPARK COLUMN PLASMA DYNAMIC MODEL

Final Report

200008O4060

Submitted to
DEPARTMENT OF THE NAVY
Office of Naval Research

Submitted by
**MATHEMATICAL
SCIENCES
NORTHWEST, INC.**

DTIC
ELECTE
NOV 1 6 1984

E

September 1984

84 10 31 120

REPORT DOCUMENTATION PAGE

READ INSTRUCTIONS
BEFORE COMPLETING FORM

1. REPORT NUMBER	2. GOVT ACCESSION NO.	3. RECIPIENT'S CATALOG NUMBER
C.11.253.01	AD-A147 954	

4. TITLE (and Subtitle)	5. TYPE OF REPORT & PERIOD COVERED
Spark Column Plasma Dynamics Model (A First Principles Model for Laser Triggered Spark Gaps)	Final Report 1 June 1983 – 31 August 1984
	6. PERFORMING ORG. REPORT NUMBER

7. AUTHOR(s)	8. CONTRACT OR GRANT NUMBER(s)
M. J. Kushner and R. D. Milroy	N00014-83-C-0417

9. PERFORMING ORGANIZATION NAME AND ADDRESS	10. PROGRAM ELEMENT, PROJECT, TASK AREA & WORK UNIT NUMBERS
MATHEMATICAL SCIENCES NORTHWEST, INC. 2755 Northup Way Bellevue, WA 98004	PE 61153N PTA RR024-01-01 WU NR 099-504

11. CONTROLLING OFFICE NAME AND ADDRESS	12. REPORT DATE
Office of Naval Research, Dept. of the Navy 800 North Quincy St. Arlington, VA 22217	September 1984
	13. NUMBER OF PAGES
	90

14. MONITORING AGENCY NAME & ADDRESS(if different from Controlling Office)	15. SECURITY CLASS. (of this report)
	15a. DECLASSIFICATION DOWNGRADING SCHEDULE

16. DISTRIBUTION STATEMENT (of this Report)

Approved for public release; distribution unlimited

17. DISTRIBUTION STATEMENT (of the abstract entered in Block 20, if different from Report)

18. SUPPLEMENTARY NOTES

19. KEY WORDS (Continue on reverse side if necessary and identify by block number)

- Laser Triggered Spark Gap
- Plasma Hydrodynamic Model
- Radiation Transport
- Dense Plasmas

20. ABSTRACT (Continue on reverse side if necessary and identify by block number)

In a laser triggered spark gap (or spark column) breakdown is initiated by a laser which creates a narrow preionized column between the electrodes. This small plasma column, of diameter ≈ 50 μm, expands to an arc with a diameter of 0.5-1.0 mm in less than 100 ns, and carries a current in excess of 10 kA. For many applications, the duration of the current pulse through the spark gap is only 100-200 ns and therefore is commensurate with the time required for the plasma column to expand. In order to optimize the performance, and minimize the circuit losses, of laser triggered spark gaps, it is

DD FORM 1473 1 JAN 73   EDITION OF 1 NOV 65 IS OBSOLETE

desireable to have a detailed understanding of the physics of the expansion phase of the spark. This report summarizes the first phase of development of a model to achieve that goal. We discuss a model which, from first principles, describes the growth of the arc in a laser triggered spark gap in a gas mixture of a noble gas and a diatomic molecule (e.g., Ar/H_2). The model makes no assumptions as to thermal equilibrium of the plasma column. Heavy particle hydrodynamics, electron kinetics, radiation transport, an external circuit, and skin depth affects for the penetration of the applied electric field are included in the analysis. We find that the expansion of the spark column is primarily by convection from the hot ionized core. An ionized channel of low mass density is confined within a high mass density compression (or shock) wave. The convective expansion of the core is augmented by thermal- and photo-ionization of the neutral gas at the interior of the high mass density shell. A simplified thermodynamic model for a laser triggered spark gap is also presented.

FINAL REPORT

SPARK COLUMN PLASMA DYNAMIC MODEL

N0014-83-C-0417

June 1983-August 1984

Submitted to

DEPARTMENT OF THE NAVY
Office of Naval Research
Arlington, Virginia

By

Mathematical Sciences Northwest, Inc.
2755 Northup Way
Bellevue, Washington 98004
(Internal Contract No. 11.253.)

Principle Investigators:

M. J. Kushner and R. D. Milroy

September 1984

SUMMARY

In a laser triggered spark gap (or spark column) breakdown is initiated by a laser which creates a narrow preionized column between the electrodes. This small plasma column, of diameter ≈ 50 μm, expands to an arc with a diameter of 0.5–1.0 mm on a time scale of 100 ns, and is capable of carrying a current in excess of 10 kA. During the expansion phase, the resistance of the plasma column decreases from many kilo-ohms to as little as a few tenths of an ohm. For many applications, the duration of the current pulse through the spark gap is only 100–200 ns and therefore is commensurate with the time required for the plasma column to expand. Therefore during the time of interest, the spark column changes from being a dominant resistive loss to being a lossless circuit element in comparison to the load. In order to optimize the performance, and minimize the losses, of laser triggered spark gaps operating under these conditions, it is desireable to have a detailed understanding of the physics of the expansion phase of the spark. This report summarizes the first phase of development of a model to achieve that goal. We discuss a model which, from first principles, describes the growth of the arc in a laser triggered spark gap in a gas mixture of a noble gas and a diatomic molecule , (eg.: Ar/H_2). The model makes no assumptions as to thermal equilibrium of the plasma column. Heavy particle hydrodynamics, electron kinetics, radiation transport, and an external circuit are included in the analysis. Skin depth affects for the penetration of the applied electric field into the plasma are also included. Results from the model are discussed. We find that the expansion of the spark column is primarily by convection from the hot ionized core. An ionized channel of low mass density is confined within a high mass density compression (or shock) wave. The convective expansion of the core is augmented by thermal- and photo-ionization of the neutral gas at the interior of the high mass density shell. Based on the results of the model, and a thermodynamic analysis, a simple thermodynamic model for a laser triggered spark gap is presented.

CONTENTS

v

SECTION I

INTRODUCTION

Spark gaps are traditionally triggered by overvoltage or by internal auxiliary electrodes. The use of lasers as trigger sources for spark gaps has significant advantages over these methods[I.1-I.9] Laser triggering of spark gaps has been demonstrated as a method whereby jitter can be minimized. For applications where many spark gaps must be triggered simultaneously, laser triggering provides a method whereby this can be accomplished.

In laser triggered spark gaps, a laser is used to initiate the electron avalanche and breakdown of the gas. A laser with sufficient intensity to ionize the gas is focused between the electrodes of the device. (See Fig. I-1) Although the potential across the spark gap may be insufficient to cause self breakdown, once a plasma column is initiated by the laser, the voltage is sufficient to sustain and expand the column. The duration, location and intensity of the laser can be carefully controlled, and therefore so can the time of breakdown of the spark gap.

Although many systematic studies of laser triggered spark gaps have been performed[I.1-I.9] and some modeling has been done[I.4,I.10], a first principles model of a laser triggered spark column has not been presented. A first principles model would treat all the basic phenomenon without making any apriori assumptions as to the thermodynamic state of the gas, and would include hydrodynamics, electron and heavy particle kinetics, radiation transport and an external circuit. Development of such a model is described in this report. We have attempted to fully describe all the pertinent physics in the plasma column without prejudice to a particular preconceived notion of the dominant processes. Although this method is not the most computationally expedient technique, it is the most revealing.

Reference is made in this report to experimental measurements. These measurements were made under contract to the Naval Surface Weapons Center (Contract N60921-83-C-A057) concurrent to the development of this model. We acknowledge the support and advice of NSWC in the experimental program.

The model is described in detail in Sec. II. Simulated spark column characteristics are discussed in Sec. III. (We use the phrases "spark gap" and "spark column" synonymously.) The rates of arc formation and expansion are discussed in Sec. IV. The simulation of interferograms from results of

the model, to compare with experimental data, is discussed in Sec. V.
Based on the results of the experimental and theoretical studies, a simple
thermodynamic model for a laser triggered spark gap is described in
Sec. VI.
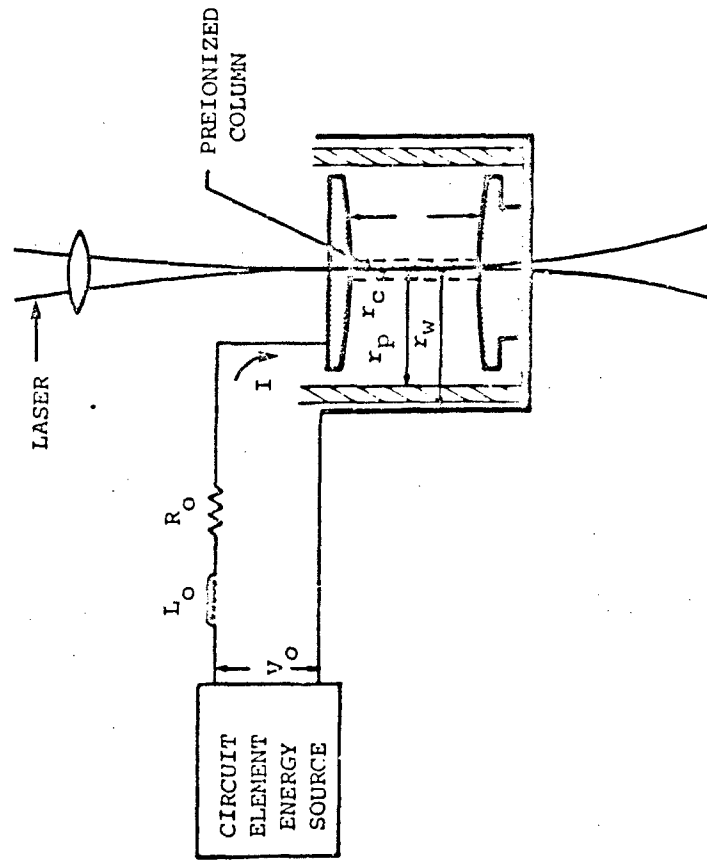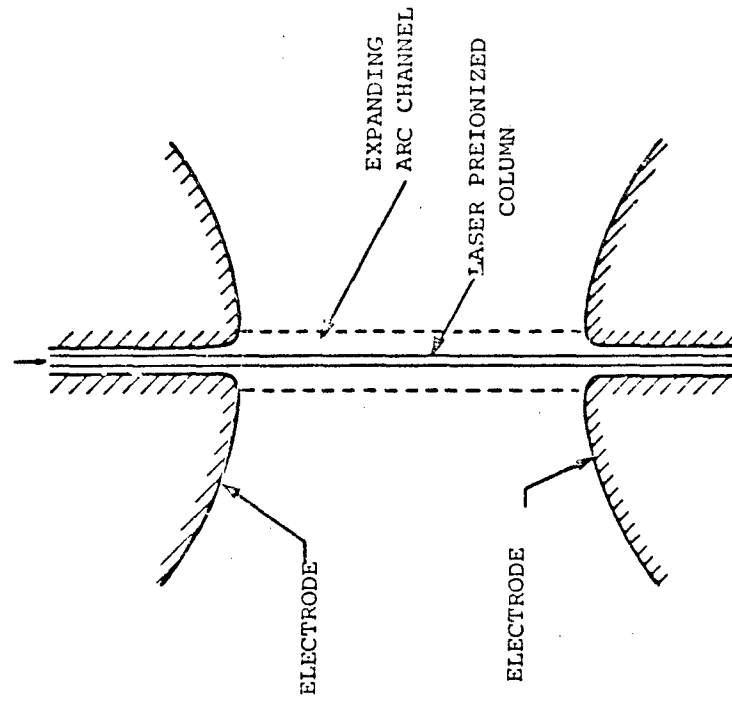
Figure I-1. Geometry for Laser Triggered Spark Column

84 08742

I-3

References for Section I

I.1) L.P. Bradley and T.J. Davies, IEEE J. Quant. Elect. QE-7, 464 (1967)

I.2) K.Harsch, H. Salzmann and H. Strohwald, Phys. Lett. A 55, 153 (1975)

I.3) A.G. Akmanov, L.A. Rivlin and V.S. Shil dyaev, JETP Lett. 8, 258 (1968) I.4) A.H. Guenther and J.R. Bettis, J. Phys. D 11, 1577 (1978)

I.5) W.R. Rapoport, J. Goldhar, and J.R. Murray, IEEE Trans. Plasma Sci. PS-8, 167 (1980)

I.6) J.R. Woodworth, R.G. Adams, and C.A. Frost, IEEE Trans. Plasma Sci. PS-10, 257 (1982)

I.7) J.R. Woodworth, C.A. Frost and T.A. Green, J. Appl. Phys. 53, 4734 (1982)

I.8) J. Goldhar, W.R. Rapoport, and J.R. Murray, IEEE J. Quantum Elect. QE-16, 235 (1980)

I.9) R. A. Dougal and P.F. Williams, J. Phys. D. 17, 903 (1984)

I.10) R. A. Dougal and P.F. Williams, J. Phys. D. (to be published).

SECTION II

DESCRIPTION OF THE MODEL

The model explicitly treats a spark column with an initial gas mixture of argon and molecular hydrogen. The energy levels included in the model, discussed below, were chosen accordingly for these species. Sparks in other gas mixtures though, can be approximated by scaling the energy levels and atomic masses used in the model from those of argon and hydrogen to those of the desired species. To approximate a diatomic molecule other than hydrogen, the mass of the desired molecule (and atomic constituient) is used in place of that of hydrogen where-ever mass appears in the model. The energy levels of molecular hydrogen, and their excitation rates, remain unchanged. The energy levels of the atomic constituient are scaled in the same fashion as that for substituting a different rare gas for argon.

To approximate a rare gas other than argon, the same mass substitution as described above is used. The appropriate electron momentum transfer cross section, thermal conductivity, and ionization potentials for the new gas are also used. The energy levels appearing in the code, selected for argon, are scaled in the following manner. The threshold energy of the first excited state is revised to that of the new rare gas. The ionization potential of the first excited state is then used as the scaling parameter. The separation in energy between adjacent levels is increased or decreased in the ratio of the ionization potential of the first excited state for the desired rare gas as compared to that of argon. The revised values of the energy levels are used in the calculation of excitation rates as required.

II.A. Heavy Particle Collisions

The importance of heavy partical collisions which result in the change in the level of excitation of one of the collision partners is particularly important with respect to expansion of the arc. The arc can expand by only one of three mechanisms. A partially ionized fluid element can convect from an inner radial point to an outer radial point, electrons can diffuse from an inner radial point to an outer radial point, or local sources can provide the seed electrons required for avalanching and subsequent rapid ionization of the gas. Two major local sources exist for these seed electrons; photoionization and thermal ionization.

As the gas temperature is raised in the core of the plasma column, the increase in thermodynamic pressure provides the driving force for an expansion wave to propagate radially outwards. At the outer limit of the expansion wave is a shock or compression wave. The compression wave is a thin region of gas with a mass density that is large as compared to the quiescent gas beyond the shock. To a good approximation, this gas undergoes an adiabatic compression and therefore has an associated increase in gas temperature. For a $\Delta\rho/\rho_o$ (ie.: change in mass density divided by the initial gas density) in the compression wave larger than 3, the gas temperature is increased to a value in excess of 1000 K. At these temperatures thermal ionization of the gas (as opposed to direct electron impact ionization) is no longer a process that can be ignored. Although the rate of thermal ionization is many orders of magnitude less than that by electron impact ionization, its importance is manifested by the fact that in the absence of free electrons (and ignoring for the moment photoionization), thermal ionization is the only local source of electrons in this region. Once local free electrons are generated by thermal ionization, and in the presence of a sufficiently large applied electric field, the more rapid rate of electron impact ionization dominates that of the thermal ionization and initiates a local electron avalanche. The non-convective expansion of the plasma column progresses radially outward as the electron density of the newly avalanched region approaches that of the core of the plasma. The electron avalanche also serves to rapidly heat the heavy particles, thereby raising the local thermodynamic pressure and perpetuating the convecting expansion wave.

Concurrent to thermal ionization in the adiabatically compressed shock, thermal dissociation and vibrational excitation also occur. Locally, thermal dissociation and vibrational excitation are not important in directly providing an impetus for the electron avalanche to occur. The importance of thermal dissociation is manifested indirectly by changes in electron transport properties that may occur as a result of the relative change in atomic and molecular densities. For example, electron impact excitation of vibrational modes of the molecular species is one of the more efficient processes by which electrons lose energy and hence by which the electron temperature is constrained to a relatively low value. If in the adiabatically heated region a large fraction of the molecular species is thermally dissociated, the rate at which electrons lose energy as a result of vibrational excitation will be reduced. This reduction enables a higher average electron temperature, a larger rate of electron impact ionization, and therefore a more rapid avalanche of the gas. Analogously, the importance to the avalanche process of thermal vibrational excitation of the molecular species is not direct; rather it is an indirect effect

manifested by changes in the rate of electron impact ionization. The ionization potential of a vibrationally excited species is smaller than that of the ground state molecule by a value equal to that of the vibrational excitation energy. For a given electron temperature, the rate of ionization of the vibrationally excited molecule is therefore larger than that of the ground state molecule. A large fraction of molecules vibrationally excited by thermal collisions can accelerate the avalanche process by providing a reservoir of molecules with a lower ionization potential than that of the ground state molecules. Although not direct contributers to the avalanche process, thermal dissociation and excitation of the molecular species can indirectly be responsible for a rapid rate of electron avalanche by the influence the products of these processes have on the rate of electron impact ionization.

The rate of thermal dissociation of molecular species in the adiabatically heated gas was obtained from the literature and is given in Table II-2. The rate of thermal ionization was approximated as being gas kinetic with an Arrhenius factor $\exp(-E_i/kT_g)$, where E_i is the ionization potential of the heavy particle and T_g is the local gas temperature.

II.B. Photoionization and Radiation Transport

Photoionization, in analogy to thermal ionization, is not, on an absolute scale, an important source of ionization. The importance of photoionization is that it provides a local source of ionization in the neutral gas exterior to the plasma column. As discussed above, local sources of ionization, independent of local electron collision processes, are necessary to provide the seed electrons required for an electron avalanche. An electron avalanche initiated by local sources of ionization in once neutral gas is the only non-convective mechanism by which the arc may increase its radius, and is the only mechanism by which new mass can be entrained into the expanding core.

The radiation which produces photoionized seed electrons in the region exterior to the arc originates in the plasma within the arc. The flux of radiation at location $\vec{r}$ of frequency ν, $\Phi(\vec{r},\nu)$, resulting from volumetric sources of radiation at location $\vec{r}'$, $S(\vec{r}',\nu)$, is given by

$$\Phi(\vec{r},\nu) = \int S(\vec{r}',\nu)\frac{\exp\left[-\int_{\vec{r}'}^{\vec{r}} \alpha_i(\vec{r}'',\nu)d|\vec{r}''-\vec{r}'|\right]}{4\pi|\vec{r}'-\vec{r}|^2} d^3\vec{r}' \qquad [II-1]$$

where $\alpha(\vec{r}'',\nu)$ is the photon absorption coefficient for frequency ν at location $\vec{r}''$. The integral in Eq. II-1 (called the photon transport integral) has, in general, no analytic solution if either the source function or absorption coefficient are complex functions of radius. For our conditions, $S(\vec{r},\nu)$ and $\alpha(\vec{r},\nu)$ are not functions of a single variable (eg.: temperature) but rather represent the sum of many processes which depend on the electron density and temperature, and the density of a large number of excited states. The integral in Eq. II-1 must therefore be performed numerically for an "exact" solution. For conditions where either $S(\vec{r},\nu)$ or $\alpha(\vec{r},\nu)$ change rapidly for the time scale of interest, repeated numerical evaluation of Eq. II-1 is costly and approximate solutions to Eq. II-1 must be used. Approximate solutions can be obtained provided that $S(\vec{r},\nu)$ and $\alpha(\vec{r},\nu)$ are constant over some finite region, or the integral in the exponent in Eq. II-1 is neglibly small. Both of these criteria hold to some extent for our conditions and are exploited to obtain approximate solutions.

To a good approximation, photons generated within the plasma column can be classified as being optically thick or optically thin. Optically thick photons are those photons that have a high probability of being absorbed over the path lengths of interest. For our conditions, these are photons of sufficiently high energy that they are capable of ionizing ground state species. Optically thin photons are those photons having a low probability of being absorbed over the path lengths of interest. For our conditions, these are photons of low enough energy that they are incapable of ionizing ground state species, but are capable of ionizing excited states. These two photon groups naturally arise from the form of the photoionization cross section and the energy separation of excited states.

For hydrogenic levels, the photoionization cross section scales as $(\epsilon/h\nu)^3$,[II.1] where ϵ is the ionization potential of the level and $h\nu$ is the photon energy. Therefore photons with energy far in excess of threshold have a small photoionization cross section for that level. Recall that for hydrogen and most noble gases, the ratio of the ionization potential for the ground state as compared to the first excited state is about 3 to 5. Therefore photons which efficiently ionize the ground state do not have a large cross section for ionizing even the first excited state. Photons that are near threshold for ionizing excited states, and

therefore have a large cross section for doing so, are not energetic enough to ionize ground states. By grouping photons into energy groups which satisfy the optically thin and optically thick criteria described above, two different approximate solutions of Eq. II-1 can be applied.

For optically thin photons, the exponential function in Eq. II-1 can be ignored and the integral reduces to

$$\Phi_k(\vec{r}) = \int \frac{S_k(\vec{r}') \, d^3\vec{r}'}{4\pi |\vec{r}' - \vec{r}|^2} \tag{II-2}$$

where $\Phi_k(\vec{r})$ is the photon flux at location $\vec{r}$ for optically thin photons grouped into an energy range denoted by k. We used cylindrical coordinates, assumed azimuthal symmetry, approximated that the axial dimension is large compared with the radial dimension and that the photon sources were constant over in a cylinder of thickness Δr and radius r. With these conditions,

$$\Phi_k(R) = \sum_i S_k[r_i] \Delta r_i \begin{cases} f\left[\dfrac{R}{r_i}\right] & r_i < R \\[2ex] \left[\dfrac{r_i}{R}\right] f\left[\dfrac{r_i}{R}\right] & r_i > R \end{cases} \tag{II-3}$$

where the summation in Eq. II-3 is over cylindrical shells. The function $f(\ell)$ is

$$f(\ell) = \frac{1}{2} \int_0^{\pi} \frac{d\phi}{\left[1 + \ell^2 - 2\ell\cos\phi\right]^{1/2}} \tag{II-4}$$

For optically thick photons, we approximate that $\alpha(r,\nu)$ is constant over the path between the point of emission and the point of observation. For the same geometry as the optically thin case, we define the parameters $a_i = r_i/R$, $b_i = \Delta r_i/R$, and $c = z/R$. The integral in Eq. II-1 reduces to

$$\Phi_k(R) = \frac{R}{\pi} \sum_i S_k[a_i] a_i b_i \int_0^{\frac{\ell}{R}} \int_0^{\pi} \frac{\exp\left[\beta_k\left[-1 + 2a_i\cos\theta + a_i^2 + c^2\right]\right]}{\left[1 + 2a_i\cos\theta + a_i^2 + c^2\right]} \, d\theta \, dc \tag{II-5}$$

$$= \frac{R}{\pi} \sum_i S_k[a_i] a_i b_i g[a_i, \beta]$$

where the average absorption coefficient of the path length of interest is

II-5

$$\beta_k = \frac{1}{|r-R|} \int_r^R \alpha_k(r')dr'$$

<div align="right">[II-6]</div>

The upper limit of integration for the axial direction is chosen such that $(\ell/R)\beta \gg 1$. The integral in Eq. II-5 was performed numerically and parameterized as function of a, and β. The results were compiled into a lookup table (function g in Eq. II-5) for use during execution of the program.

For our plasmas of interest, the absorption coefficient is the sum of two dominant terms. The first, and of lesser importance in the partially ionized phase, is inverse bremsstrahlung or free-free absorption. The absorption coeffiecient for photons of frequency ν in a plasma with temperature T is$^{(II.1)}$

$$\alpha_{FF}(\nu) = \sum_i \left[\frac{4}{3} \left(\frac{2\pi}{3kT} \right) \frac{n_e N_i Z_i^2 e^6}{hcm_e^{3/2} \nu^3} g_{ff} \right] \left[1 - \exp\left(\frac{-h\nu}{kT} \right) \right] \ cm^{-1}$$

<div align="right">[II-7]</div>

where the factor $g_{ff} \approx 1$, N_i is the density of ion i, and Z_i is the ionization state of ion i. The second and dominant absorption mechanism during the partially ionized phase is bound-free electron transitions, or photoionization. For hydrogenic states, the photoionization absorption coefficient for frequency ν is approxmately

$$\alpha_p(\nu) = \sum_{i,j} 7.9 \times 10^{-18} \ N_{ij} \left[\frac{\epsilon_{ij}^I}{h\nu} \right]^3 \begin{cases} 0 & \epsilon_{ij}^I < h\nu \\ 1 & \epsilon_{ij}^I \geqslant h\nu \end{cases}$$

<div align="right">[II-8]</div>

where N_{ij} is the density of species i excited to level j and ϵ_{ij}^I is the ionization potential for that state. In practive, photons were grouped into energy bins with widths of a few electron volts. When doing so the absorption coefficient for a particular energy bin was the average value of of Eq.s II-7 and II-8 for the range of energy of interest. When the plasma becomes fully ionized, and at longer wavelengths. inverse bremsstrahlung becomes the more important absorption mechanism.

I.C. Radiation Source Terms

Although line radiation is included a.3 an energy loss mechanism (ie.: spontaneous emission), radiation transport in calculated only for the continuum component of the spectrum. The radiation source function $S(\vec{r}, \nu)$

(photons/cm^3-s) for this continuum component results from free-bound radiative recombination and bremsstrahlung. The former source is the more important source at lower electron temperatures and densities. The latter is the more important source at higher electron temperatures and densities. Assuming hydrogenic levels, the source function for free bound radiation resulting from recombination of electrons with temperature T_e recombining into a level with ionization potential ϵ_o and emitting radiation with energy between ϵ_k and ϵ_{k+1} is[II.1]

$$S_k = \sum_{\epsilon_k > \epsilon_{oj}} n_e N^+ A[T_e] \int_{\frac{2}{m_e}\{\epsilon_k - \epsilon_{oj}\}}^{\frac{2}{m_e}\{\epsilon_{k+1} - \epsilon_{oj}\}} \frac{\exp(-\beta x)\, dx}{\left[\frac{1}{\gamma^2} + x\right]} \qquad [II-9]$$

where the summation is over all atomic and molecular states in the plasma which satisfy the energy criteria $\epsilon_k > \epsilon_{oj}$, $\gamma^2 = m_e/(2\epsilon_{oj})$, and $\beta = m_e/(2kT_e)$. N^+ is the density of atoms in the next higher ionization state than the level to which recombination is occuring and $A(T_e)$ is a normalization constant to insure that the sum of photon sources equals the rate of radiative recombination.

$$\sum_k S_k = \sum_{i,j} n_e N_i^+ r_{ij}^r . \qquad [II-10]$$

The source function for free-free (bremstrahllung) radiation resulting from electrons with temperature T_e colliding with ions of charge state Z and density N_i^Z and emitting radiation with energy between ϵ_k and ϵ_{k+1} is[II.2]

$$S_k = \sum_i n_e N_i^Z r[Z, T_e, \epsilon_k, \epsilon_{k+1}] \qquad [II-11]$$

$$r[Z, T_e, \epsilon_k, \epsilon_{k+1}] = \qquad [II-12]$$

$$\frac{2\pi}{[\pi k T_e]^{3/2}} \left[\frac{2}{m_e}\right]^{1/2} \int_{\epsilon_k}^{\infty} \xi\, \sigma_{ff}[Z, \xi, \epsilon_k, \epsilon_{k+1}]$$

$$\cdot \exp\left[-\frac{\xi}{kT_e}\right] d\xi$$

$$\sigma_{ff}[Z, \xi, \epsilon_k, \epsilon_{k+1}] = \qquad [II-13]$$

$$\frac{8}{3} \frac{2\pi Z^2 e^2}{hc} \left[\frac{e^2}{m_e c^2}\right]^2 \frac{mc^2}{\xi} \int_{\epsilon_k}^{\min[\xi, \epsilon_{k+1}]} \frac{1}{u} \ln\left[\frac{\left[\xi^{1/2} - (\xi-u)^{1/2}\right]^2}{u}\right]$$

$$\cdot \frac{\xi^{1/2}}{(\xi-u)^{1/2}} \frac{1 - \exp\left[-\dfrac{\beta}{\xi^{1/2}}\right]}{1 - \exp\left[-\dfrac{\beta}{(x-u)^{1/2}}\right]} \, du$$

$$\beta = \frac{4\pi^2 Z e^2}{h \left[\dfrac{2}{m_e}\right]^{1/2}} \tag{II-14}$$

In Eqs. II-11 to II-14, $r(Z, T_e, \epsilon_k, \epsilon_{k+1})$ is the rate constant for the process by Maxwellian electrons with temperature T_e and $\sigma_{ff}(Z, \xi, \epsilon_k, \epsilon_{k+1})$ is the analogous cross section for a single electron having energy ξ. Eq. II-12 is the averaging of the cross section for energy ξ over the Maxwellian electron distribution function.

II.D. Hydrodynamic and Thermodynamic Equations

     In this section, we will describe the hydrodynamic and thermodynamic equations used to model the plasma column. These equations treat the plasma as a single fluid but with two temperatures. The nearly fully ionized core in the center of the arc is close to being in thermal equilibrium and a single temperature might suffice. Exterior to the core, the electrons and heavy particles are not in thermal equilibrium and therefore two temperatures are required, the electron temperature and the heavy particle, or gas, temperature. Conceptually, each temperature is associated with a given mass fraction. In similar situations, one would require two fluids to accurately describe the pertinent hydrodynamics, electrons and heavy particles. For our conditions, though, the two particles are sufficiently well coupled that a single fluid convective velocity suffices. This fact results from the high ion density, low rate of diffusion, and high heavy particle collision frequency.

     For our conditions, the ion density is sufficiently high that electron transport is accurately described by the ambipolar approximation. Using this approximation (see below for details), the diffusive motion of electrons is constrained to that of the ions, the rate of which is increased as a result. The region of charge separation, though, is small compared to our spatial resolution. Therefore the density of electrons and

ions are locally equal. The low rate of diffusion for all particles, as compared to the convective motion, insures that the ions convect at the same velocity as other heavy particles. The high collision frequency between heavy particles insures that all heavy particles can be described with a single temperature.

In the ambipolar diffusion approximation, the radial electric field can be written as[II.1]

$$E_r = \frac{\nabla P_e}{e n_e} \qquad [II-15]$$

where P_e is the thermodynamic electron pressure and n_e is the electron density. The force of this electric field acts only on the ions. However, due to the high collision frequency between heavy particles, the momentum acquired by the ions is distributed among both ions and neutrals in a nearly uniform fashion. The contribution of the radial electric field to momentum equation is therefore weighted by the mass fraction of ions ... ied by their charge state.

With a single fluid, albiet with multiple temperatures, there is no relative motion between species. The convective velocity, though, is sufficiently large that the linear dimension of the region of interest may change by more than an order of magnitude during the discharge pulse while the entrained mass changes by a significantly smaller value. Under these conditions, a Lagrangian formulation of the transport equations is appropriate. Using this formulation, the fluid mass within each computational cell remains constant while the cell boundaries move with the convective velocity. In this manner, the density of mesh points tends to increase in regions of compression where gradients are likely to be large.

The fluid continuity and momentum conservation equations used in the model are

$$\frac{d\rho}{dt} = -\frac{\rho}{r}\frac{\partial}{\partial r}(ru) \qquad [II-16]$$

$$\frac{du}{dt} = -\frac{1}{\rho}\frac{\partial}{\partial r}\left[\left[\frac{\sum_i z_i \rho}{\sum_i \rho}\right]\nabla P_e + \nabla P\right] - \frac{1}{\rho}\frac{B}{4\pi}\frac{1}{r}\frac{\partial}{\partial r}(rB) \qquad [II-17]$$

In Eq. II-17, the sum is over heavy species and Z_i is the charge state of species i. The last term in Eq. II-17 is due to the effect of self generated electromagnetic fields and is the source of the compressive force

in "pinch" plasmas. For our collisionally dominated conditions, this effect is not important.

Separate energy equations were written for the electrons and the heavy particles. Energy is coupled into the plasma through the acceleration of electron by the applied electric field. Heavy particles are heated by collisions with electrons. The energy equations are coupled to the momentum equation through the pressure gradient.

The electron energy conservation equation is

$$\frac{d\left[\frac{3}{2}n_e kT_e\right]}{dt} = \qquad\qquad\qquad [II-18]$$

$$- P_e \frac{1}{r}\frac{\partial}{\partial r}(ru) - \frac{1}{r}\frac{\partial}{\partial r}\left[r\lambda_e \frac{\partial T_e}{\partial r}\right] + J^2/\sigma$$

$$- \frac{3}{2}n_e k \left(T_e - T_g\right) \sum_i N_i \left[\frac{2m}{M_i}\right] \nu_i - \sum_{i,j} \epsilon_{ij} n_e \left[N_i - N_j \exp\left[-\frac{\epsilon_{ij}}{kT_e}\right]\right] r_{ij}$$

$$- \sum_i n_e N_i r_i^I \left[\frac{3}{2}kT_e + \epsilon_i^I\right] + \sum_{i,j} n_e^2 N_i^+ r_{ij}^C \left[\frac{3}{2}kT_e + \epsilon_j^I\right]$$

$$- \sum_{i,j} n_e N_i^{z+} r_{ij}^r \left[\frac{3}{2}kT_e\right] - \sum_i \kappa n_e z_i^2 N_i T_e^{1/2}$$

$$+ \sum_i \int \Phi(\nu)\sigma_i^I(\nu)\left[h\nu - \epsilon_i^I - \frac{3}{2}kT_e\right] d\nu.$$

The single subscript M_i refers to a particular state of a given species and the double subscript r_{ij} for a rate constant or energy refers to transitions or energy differences between species i and j. In Eq. II-18, P_e is the partial pressure of the electron gas, λ_e is the electron thermal conductivity, J is the current density, σ is the electrical conductivity, ϵ_{ij} is the energy separation between species i and j, and ϵ_i^I is the ionization potential of species i. The rate constant for excitation of N_i to N_j is r_{ij}, the rate constant for ionization of N_i is r_i^I, the rate constant for collisional radiative recombination of ion N_i^{z+} to form species $N_i^{(z-1)+}$ is r_{ij}^C and the analogous rate constant for radiative recombination is r_{ij}^r. ν_i is the electron collision frequency, and $\sigma_i^I(\nu)$ is photoionization cross section of species i for frequency ν.

The terms in Eq. II-18 are for heating of the electrons by adiabatic compression of the electron component of the fluid, thermal conduction,

joule heating, thermalization of electrons with the heavy particles, inelastic and superelastic excitation collisions with heavy particles, ionization collisons with heavy particles, electron heating due to collisional radiative recombination, energy loss due to radiative recombination, energy loss due to bremsstrahlung radiation, and energy inputs to the distribution resulting from photoionization. In the term for bremsstrahlung loss the constant $\kappa = 10^{-13}$ eV$^{1/2}$-cm^3/s which is small compared to joule heating. The thermal conduction term serves to smooth the electron temperature distribution as a function of radius, however because electron transport is dominated by collisions with heavy particles, this term is not a dominant contributor to the total.

Recombination heating is the transfer of thermal and potential energy of a recombining electron to a second electron during the collision which occurs during collisional radiative recombination. Radiative recombination differs from collisional radiative recombination in that in the former process the kinetic and potential energy of the recombining electron is released only by emitting a photon. Recombination heating is a particularly important term. In the core of the arc where quasi-steady state conditions are obtained, the rate of recombination is equal that of ionization, and the dominant form of recombination is collisional radiative. For illustrative purposes, assume that the second colliding electron carries off on the average twice the thermal energy. Then for an electron density of 10^{19} and electron temperature of 4 eV, the rate of recombination heating is 15 GW/cm^3, which is comparable to the rate joule heating, approximately 90 GW/cm^3. Recombination heating is not a true heat source in the sense of being an external source of energy. Recombination heating returns to the electron distribution the kinetic energy of electrons previously "lost" as a result of inelastic ionizing collisions. This energy is stored as the potential energy of electrons in the continuum relative to the excitation level of the state from which the ionization occured.

The heavy particle energy conservation equation is

$$\frac{d\left[\rho c_p T_g\right]}{dt} =$$

[II-19]

$$- p\,\frac{1}{r}\frac{\partial}{\partial r}(ru)\ \frac{1}{r}\frac{\partial}{\partial r}\left[r\lambda_g\frac{\partial T_g}{\partial r}\right]$$

$$+ \frac{3}{2}n_e k\left[T_e - T_g\right]\sum_i N_i\left[\frac{2m}{M_i}\right]\nu_i$$

$$- \sum_{i,j,k,l} \epsilon_{ijkl} \left[N_i N_j - N_k N_l \exp\left(\frac{\epsilon_{ijkl}}{kT_g}\right) \right] r^H_{ijkl}$$

where c_p is the heavy particle specific heat, λ_g is the heavy particle thermal conductivity and ν_i is the electron collision frequency with species i. The terms of j are for heating from adiabatic compression, heat transport due to thermal conduction, and joule heating by collisions with hot electrons. In the last term of j, for changes in internal energy due to heavy particle collision processes, r^H_{ijkl} is the endothermic rate at which reactants i and j collide, resulting in product species k and l. The activation energy for the process is ϵ_{ijkl}. The reverse exothermic reaction results in heating of the gas. Examples of these heavy particle collision processes are

$$H_2^{(i)} + M^{(j)} \rightarrow H^{(k)} + H^{(k)} + M^{(l)}, \qquad \epsilon_{ijkl} = 4.5 \text{ eV} \qquad \text{[II-20]}$$

$$H_2(v=0)^{(i)} + M^{(j)} \rightarrow H_2(v=1)^{(k)} + M^{(l)}, \epsilon_{ijkl} = 0.5 \text{ eV} \qquad \text{[II-21]}$$
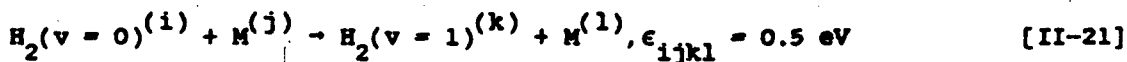
where M is any second or third body. The forward heavy particle reactions are especially important in the dissociation of the molecular species. This results from the rapid heating of the gas by electron collisions and the relative inefficiency with which electrons dissociate molecules as compared to heavy particles of the same temperature.

II.E. Kinetic Equations

The hydrodynamic and thermodynamic equations described in the previous section yield the fluid density, heavy particle temperature, and electron temperature at a given radial point. The specific properties required for solution of the hydrodynamic and thermodynamic equations (ie.: energy loss rates, electrical conductivity, thermal conductivity) are obtained by solution of kinetic equations which provide the density of individual species within the given computational cell. From these densities the necessary thermodynamic properties and reaction rates are obtained. The species included in the model, as functions of radial position and time, are listed in Table II-1. For atomic neutral and ionic species, the notation (n) in Table II-1 indicates an excited state. For hydrogen, the first ten states of atom were used. Due to the large number of excited states for neutral and ionized argon, actual states were grouped into pusedo states, comprising the actual states lying inside an energy interval approximately 1500 cm^{-1} to 3000 cm^{-1} wide. This represents a

somewhat coarser selection of states than that used for calculation of partition functions. (See Sec. VI.) The statistical weights of the pseudo states are the sum of the statistical weights of the actual levels falling within the energy interval. The energy levels used for Ar I to Ar VI are listed in Table II-3. Although properties are included in the model for up to five times ionized argon, most of the results discussed here are for calculations where the highest ionization state included is Ar III. The density of Ar III for these conditions is sufficiently small that higher ionization states are not necessary.

For computation of the electron temperature both vibrational and electronic states of H_2 were included. However only the v = 1 vibrational state and H_2^* ($\epsilon = 8.85$ eV) electronic state were carried as kinetic variables. For our collisionally dominated plasmas, the lifetimes of these states are very short as they relax to the ground states (or first vibrational state) quickly. Inclusion of the electron impact process for excitation of the state while not including the state as a kinetic variable is equivalent to having an instantaneous relaxation of the state.

The processes included in the kinetics portion of the model are summarized in Table II-2. Conservation equations for each species were written. The entries in Table II-2 are for processes which change the density of a particular species as a result of electron or heavy particle collisions. The change in density of a particular species due to non-collisional processes (ie.: convection) is a quantity derived from the hydrodynamic equation for heavy particle density. In the Lagrangian formulation, the hydrodynamic equations provide the mass density in each computational cell, while maintaining a constant total mass in the cell. Therefore the fractional change in mass density in the cell, resulting from expansion or contraction of the cell boundaries, manifiests a similar fractional change in the particle density of each species within the cell. Therefore a correction term for convective effects is included in the conservation equation for each species. A typical conservation equation for a kinetic species in the model is

$$\frac{\partial H_i}{\partial t} = \tag{II-22}$$

$$\sum_j n_e \left(r_{ji} H_j - r_{ij} H_i \right) - n_e r_i^I H_i + n_e \left(r_i^r + r_i^{cr} n_e \right) H^+$$

$$+ n_e \left[r_d^r H_2^+ \left(\delta_{i1} + \delta_{in} \right) + 2 r_d \left(H_2 + H_2(v) \right) \delta_{i1} + r_d H_2^* \left(\delta_{1i} + \delta_{ni} \right) \right]$$

II-13

$$-\sum_k N_k \left[\sum_{j>i} \sum_{l<j} \left[r_{ji}^{h} H_j - r_{ij}^{h} H_i \right] \right] + 2\, r_{dk}^{H_2} H_2 \delta_{1i} + 2\, r_{dk}^{H_2(v)} H_2(v)\delta_{1i}$$

$$+ 2\, r_{dk}^{H_2^*}\left[\delta_{1i} + \delta_{ni}\right] + r_{dk}^{H_2^+}\delta_{1i} - \sum_l r_k^{ra} H_l H_i$$

$$+ \frac{H_i}{\rho}\frac{d\rho}{dt}$$

In Eq. II-22, δ_{ni} denotes that the process only pertains to the hydrogen excited state $n = i$ and N_k denotes a third body which has associated with it a unique rate constant also having subscript k. The following terms in Eq. II-22, in order of presentation, have rate constants that are function of electron temperature: electron excitation of H_i from level H_j (rate constant r_{ji}); electron collisional relaxation of H_i to H_j (r_{ij}); electron impact ionization of H_i (r_i^{I}); recombination of H^+ populating H_i by radiative recombination (r_i^r) and by collisional radiative recombination (r_i^{cr}); dissociative recombination of H_2^+ populating $H(1)$ and a higher excited state (r_d^r); electron impact dissociation of H_2, $H_2(v)$, and H_2^* (r_d). The following terms in Eq. II-22, in order of presentation, have rate constants that are functions of heavy particle temperature: collisional quenching by heavy particles of a higher lying level j to H_i (r_{ji}^{h}) and of H_i to a lower level j (r_{ij}^{h}); thermal dissociation of H_2, $H_2(v)$, H_2^{**}, and H_2^+ (rate constants $r_{dk}^{H_2}$, $r_{dk}^{H_2(v)}$, $r_{dk}^{H_2^*}$, $r_{dk}^{H_2+}$); and reassociation of H atoms to make H_2. The last term in Eq. II-22 is the correction to the density of H_i resulting from convection.

II.P. Circuit Equations

From a system point of view, the spark column is merely a reactive element in a discharge circuit. The driving force for the kinetics and hydrodynamics for the spark column is the applied electric field from the discharge circuit. The coupling between the microscopic properties of the spark column and the measureable macroscopic parameters is described by the external circuit model.

A schematic of the external circuit model is in Fig. II-1. The capacitance of the equivalent external circuit is C_E, its inductance L_E, and its apparent resistance R_E. The spark column of length ℓ has resistance R_S and inductance L_S. The parallel resistance R_p ($\approx 1000\ \Omega$) is that associated with diagnostic probes. The resistance of the plasma column is

$$R_S = \frac{\ell \int_0^{d/2} 2\pi r \frac{j(r)^2}{\sigma(r)} \, dr}{I^2} \qquad \text{[II-23]}$$

where d is the column diameter, $j(r)$ is the current density, $\sigma(r)$ is the electrical conductivity and I is the total current through the column. The column resistance is equivalently written as

$$R_S = \frac{\ell}{\int_0^{d/2} \frac{n_e(r)e^2}{m_e \nu_c} 2\pi r \, dr} \qquad \text{[II-24]}$$

where $n_e(r)$ is the electron density, m_e is the electron mass, and ν_c is the electron collision frequency. The spark column inductance is

$$L_S = \frac{2e}{I^2} \int_0^{d/2} \frac{B^2(r)}{4} \, dr + \frac{\mu_o}{2\pi} \ell n \left[\frac{R_C}{(d/2)} \right] \qquad \text{[II-25]}$$

where the magnetic field at location r is

$$B(r) = \frac{2}{rc} \int_0^r j(r') \, 2\pi r' \, dr' \qquad \text{[II-26]}$$

In Eq. II-25, R_C is the radius of the current return path. The total current through the spark column, I, is the integral of the current density j over the cross sectional area of the plasma. The local current density is simply written as $\mu_e(r)E(r)$ where $\mu_e(r)$ is the electron mobility and $E(r)$ is the local electric field. For our conditions $E(r)$ is truely a local variable and therefore must be obtained by solution of Maxwell's equations. (That is, $E(r)$ is not necessarily V/ℓ.) The electric, or equivalently the magnetic field, applied to the spark column must "diffuse" into the interior of the plasma. This effect is known as skin depth. The local current density is therefore obtained from solution of

$$\frac{dj(r)}{dt} = u \frac{\partial j}{\partial r} + \frac{c^2}{4\pi r} \frac{1}{\partial r} \frac{\partial}{\partial r} \left[r \frac{\partial}{\partial r} \left[\frac{j(r)}{\sigma(r)} \right] \right] \qquad \text{[II-27]}$$

$$- \frac{c}{4\pi} \frac{1}{r} \frac{\partial}{\partial r} \left[r \frac{\partial}{\partial r} (u(r)B(r)) \right]$$

With the quantities defined above, the equations solved for the external circuit are

$$\frac{dV}{dt} = -\frac{I}{C_E}, \qquad \frac{dI}{dt} = \frac{V - V_p}{L_E} \qquad\qquad [II-28]$$

where the voltage drop across the plasma column is

$$\frac{dV_p}{dt} = \frac{R_p R_S}{L_S}\left[I - \frac{V_p}{R_p}\right] + R_p\left[\frac{dI}{dt} - \frac{V_p}{L_S}\right] \qquad\qquad [II-29]$$

For conditions where the L_p is small, $V_p = I(R_S R_p)/(R_S + R_p)$.

II.G Transport Coefficients

II.G.1. Electrical Conductivity and Electron Collision Frequency

The electron collision frequency enters into the model in at least three places; electrical conductivity, electron thermal conductivity, and momentum transfer to heavy particles (ie.: gas heating). In a partially ionized plasma, the electron collision frequency, ν_c, is the sum of the collision frequency with neutral particles, ν_{cN}, and with ions, ν_{cI}. The former frequency, ν_{cN}, is given simply by the product of the neutral particle density with the convolution of the momentum transfer cross section and the electron distribution function, in this case a Maxwellian characterized by the temperature T_e. The later frequency, ν_{cI}, is normally given by the Spitzer value,

$$\nu_{cI} = \sum_k Z_k N_k \; \frac{4(2\pi)^{1/2}}{3} \left[\frac{m_e}{kT_e}\right]^{3/2} \left[\frac{e^2}{4\pi\epsilon_o m_e}\right]^2 \; \ln\Lambda \qquad\qquad [II-30]$$

$$\Lambda = \frac{12\pi}{e^3}\left[\frac{\left[\frac{\epsilon_o kT_e}{Z}\right]^3}{n_e}\right]^{1/2} \qquad\qquad [II-31]$$

where the sum is over ions in the plasma having charge Z_k and density N_k. When the ion collision frequency is large compared to the neutral collision frequency, the conductivity approaches the Spitzer limit.[II.3] In this limit, the conductivity is only a first order function of electron temperature. There is a weak dependence on electron density as a result of the appearance of n_e in the expression for Λ.

The conductivity of interest is that value for motion perpendicular to the magnetic filed, $\sigma_\perp$. This value, as opposed to $\sigma_\parallel$, is used because our plasma is highly collisional and satisfies the criteria[II.3]

$$\omega_c/\nu_c = \frac{1.2 \times 10^{13} \, BT_e^{3/2}}{Z \ln\Lambda n_e} \ll 1 \qquad \text{[II-32]}$$

where ω_c is the electron cylcotron frequency, ν_c is the electron collision frequency, B is in Gauss, T_e is in eV and n_e is in cm^{-3}. For our typical values, $\omega_c/\nu_c \approx 2 \times 10^{-2}$.

The derivation of Eqs. II-28 and II-29 assumes that there are many electrons within a Debye sphere, or equivalently, $(4/3)\pi\lambda_D^3 \gg 1 \rightarrow \Lambda \gg 1$. This condition requires that $n_e \ll 3 \times 10^{18} \, T_e^{3/2} \, cm^{-3}$, where the electron temperature is in ev.[II.3] For our plasmas, this conditions is not necessarily met. A first order correction to Eq. II-30 is to replace $\ln\Lambda$, which in itself is an approximation, with the exact expression.

$$\ln\Lambda \rightarrow \int_0^\Lambda \frac{x^3}{\left(1 + x^2\right)^2} \, dx = \frac{1}{2}\left[\ln\left(1 + \Lambda^2\right) - \frac{\Lambda^2}{1 + \Lambda^2}\right] \qquad \text{[II-33]}$$

Further refinement in the value of ν_{cI} requires detailed kinetic modeling. For non-Debye plasmas, the conductivity is usually lower than the value one would calculate in the Spitzer limit. Semi-emperical refinements in this value have been made.[II.4]

II.G.2. Thermal Conductivity

Thermal conductivity enters into the calculation in both the heavy particle and electron energy equations and is a mechanism whereby spatial variations of the internal energy of the plasma are smoothed in the absence of convection. The conduction of heat in the heavy particle fluid is important only at the boundary of the hot, low density core and the relatively cold, high density shock wave. Conduction of heat from the core into the cool shock contributes to thermal ionization. Recall that it is only by thermal ionization or photo-ionization and subsequent electron avalanche that the plasma column can expand by non-convective means.

The electron thermal conductivity is a function of the electron density, temperature, and collision frequency with heavy particles.[II.1]

$$\lambda_e = \frac{2.4}{\left[\nu_{cH} + \frac{\nu_{cI}}{2^{1/2}}\right]} \frac{k^2 n_e T_e}{m_e} \qquad [II-34]$$

where ν_{cH} is the electron collision frequency with all heavy particles.

The analogous expression for heavy particles cannot be readily written. Although the thermal conductivity of a high temperature gases has been measured, we require the value for arbitrary mixtures of Ar and H_2 in non-equilibrium conditions. We therefore must resort to the first principles expression. The thermal conductivity for a mixture of heavy particles is

$$\lambda_M = \sum_s \frac{N_s \left[\frac{15}{8} N_s \left[\frac{8kT}{\pi M}\right]^{1/2} \ell_s\right] \left[\frac{9\gamma_s - 5}{15\left[\gamma_s - 1\right]}\right]}{\left[\sum_r N_r \left[\frac{2M_{sr}}{M_s}\right]^{1/2} \frac{Q_{sr}}{Q_{ss}}\right]} \qquad [II-35]$$

where N_s is the density of species s, M_s is the mass of species s, M_{sr} is the reduced mass between species s and r, γ_s is the ratio of specific heats for species s, ℓ_s is the mean free path of species s, and Q_{sr} is the collision cross section between species s and r. The sums are over all heavy species. For collisions between neutral species, the collision cross section was approximated by $Q_{sr} \approx \pi\rho_{rs}^2$, where ρ_{rs} is the Lennard-Jones parameter between speces r and s. Values for ρ_{rs} used in the model are listed in Table II-4. For collisions between neutrals and ions, a collision cross section of 10 A^2 was used. For collisions between ions, the Spitzer cross section for charged species was used.

$$Q_{rs}^{II} = 6\pi \left[Z_r Z_s\right]^2 \left[\frac{e^2}{12\pi\epsilon_o kT}\right]^2 \ell n\Lambda \qquad [II-36]$$

where Λ is as given in Eq. II-31.

The ratio of specific heats was assumed to be 5/3 for all monoatomic species. For the diatomic species H_2 and H_2^+, $\gamma = c_p/c_v$ was obtained by separately calculating c_p and c_v. The specific heat at constant pressure, c_p was obtained from the formulas and constants for the appropriate species found in Ref. II.5. The specific heat at constant volume, c_v is calculated by noting that $c_v = T(\partial S/\partial T)$ and obtaining the entropy S from the formulas

and constants in Ref. II.5.

TABLE II-1

SPECIES INCLUDED IN THE MODEL

Hydrogen:

H_2

$H_2(v)$, $v=1,2$

H_2^*

H_2, $\epsilon=8.85$ eV, 12 eV

$H(n)$, $n=1,10$

Argon:

$Ar(n)$ I, $n=1,11$

$Ar(n)$ II, $n=1,7$

$Ar(n)$ III, $n=1,6$

$Ar(n)$ IV, $n=1,5$

$Ar(n)$ V, $n=1,3$

Ar VI

Ar_2^*

Ar_2^+

Table II-2

ELECTRON IMPACT AND HEAVY PARTICLE COLLISION RATES

PROCESS	RATE[+]	REFERENCE
$e + H_2 \rightarrow H_2 + e$	a)	1
$e + H_2 \rightarrow H_2(v=1,2) + e$	a)	2, b)
$e + H_2 \rightarrow H_2^{*,**} + e$	a)	3, b)
$e + H_2 \rightarrow 2H + e$	a)	4
$e + H_2 \rightarrow H_2^+ + 2e$	$\epsilon = 15.4$ eV c),d)	5,6
$e + H_2^* \rightarrow 2H + e$	$\epsilon = 12.0$ eV	e)
$e + H_2^* \rightarrow H_2^+ + 2e$	$\epsilon = 3.4$ eV c),d)	5,6
$e + H_2^+ \rightarrow H^+ + H + e$	a)	7
$e + H(n) \rightarrow H(n) + e$	a)	8
$e + H(n) \rightarrow H(n+1) + e$	$\epsilon_n = 13.6(1/n^2 - 1/(n+1)^2)$ g)	5,6, b)
$e + H(n) \rightarrow H^+ + 2e$	$\epsilon = 13.6/n^2$ c),d)	5,6
$e + H_2^+ \rightarrow 2H$		
$e + Ar \rightarrow Ar + e$	a)	10
$e + Ar(n) \rightarrow Ar(n+1) + e$	g)	5,6
$e + Ar(n)^Z \rightarrow Ar(1)^{Z+1} + 2e$	d),g)	5,6
$e + Xe \rightarrow Xe + e$	a)	10
$e + M^{Z+} \rightarrow M^{Z+} + e$ f)	$2.9(-6)ZF(\Lambda)/(T_e^{3/2})\gamma(Z)$ 11,12	
$e + M^{Z+} \rightarrow M^{(Z-1)+}$		
$e + e + M^{Z+} \rightarrow M^{(Z-1)+} + e$		

II-21

$H_2 + M \rightarrow H + H + M$

M=Ar $6.92(-6)T_g^{-1.025}\exp(-51992/T_g)$ 13

M=H_2 $2.95(-4)T_g^{-3/2}$

M=H $2.0(-6)T_g^{-3/2}$

$M + (H_2^*, H_2(v=1)) \rightarrow M + 2H$ h)

$M + H_2^+ \rightarrow M + H^+ + H$ h)

$H_2(v=0) + M \rightarrow H_2(v=1) + M$

M=Ar $4.153(-28)T_g^{4.3}$ 11

M=H_2 $2.461(-27)T_g^{4.3}$

M=H $3.32(-10)\exp(-1369/T_g)$

$M + M \rightarrow M^+ + M + e$ $1(-16)v_{th}\exp(-\epsilon_i/kT_g)$ i)

$H^{**} + M \rightarrow H^* + M$

M=Ar,H $1(-18)$ cm^2 >j)

M=H_2 $1(-17)$ cm^2

$Ar^{**} + M \rightarrow Ar^* + M$

M=Ar,H $1(-18)$ cm^2 >j)

M=H_2 $1(-17)$ cm^2
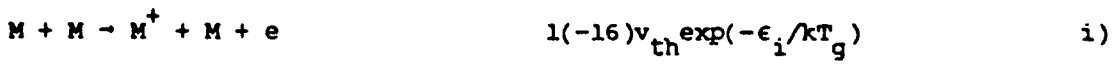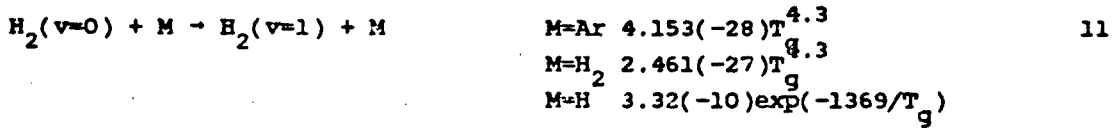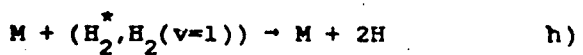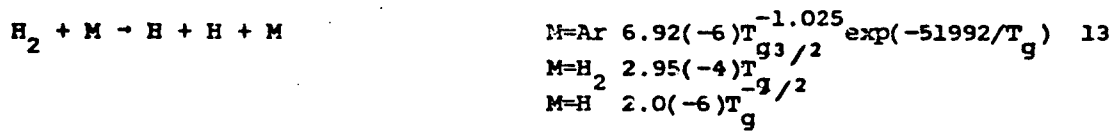
+ $5(-7) \equiv 5 \times 10^{-7}$. Rates are in units of cm^3-s^{-1} unless noted otherwise. T_e in eV, T in K

a) Cross section in indicated reference was averaged over a Maxwellian electron distribution function to obtain collision rate as a function of electron temperature.

b) Reverse rates are by detailed balance.

c) Rate is a function of threshold energy, ϵ, as indicated.

d) Subject to lowering of ionization potential.

e) Cross section and rate from Refs. 5 and 6 were used where the threshold energy is equal to the dissociation energy.

f) $\gamma(Z)$ is the Spitzer correction term and $\Lambda = 1.55(10)(T_e^3/n_e)^{1/2}$. For $F(\Lambda)$, see Sec. II-C.

g) For threshold energy, see Table II-3.

h) Same rate as for H_2 except for Boltzmann factor with which the actual dissociation energy is used.

i) ϵ_I is the ionization potential and v_{th} is the thermal velocity. See Sec. II-X.

j) Estimate

References for Table II-1

1. D. K. Gibson, Aust. J. Phys. **23**, 683(1970)

2. G. J. Schulz, Phys. Rev. **135**, A983(1964)

3. A. G. Engelhardt and A. V. Phelps, Phys. Rev. **131**, 2115(1963)

4. S. J. B. Corrigan, J. Chem. Phys. **43**, 4381(1965)

5. H. W. Drawin, European CEA Report No. FC-387, 1967; European CEA Report No. FC-383, 1966.

6. C. Deutsch, J. Appl. Phys. **44**, 1142(1973)

7. C. F. Chan, "Reaction Cross Sections and Rate Coefficients Related to the Production of Positive Hydrogen Ions". Lawrence Berkeley Laboratory LBID-632, 1983.

8. Y. Itikawa, Planet. Space Sci. **19** 993 (1971)

9. Erwin and Kung, Trans. Plasma Science **PS-11**, 266(1983)

10. L. S. Frost and A. V. Phelps, Phys. . . '. **136**, A1538(1964)

11. M. Mitchner and C. P. Kruger, Jr., _Partially Ionized Plasmas_, Wiley, New York (1973).

12. N. Cohen and J. F. Bott, "Review of Rate Data for Reactions of Interest in HF and DF Lasers", Aerospace Corporation #SD-TR-82-86, Oct. 1982.

13. V. N. Kondratiev, _Rate Constants of Gas Phase Reactions_, NTIS COM-72-10014, Jan 1972.

TABLE II-3

Argon Psuedo State Energies and Degeneracies

Ar I (I.P.= 126881. cm^{-1})		Ar II (I.P.= 222434. cm^{-1})	
Energy (cm^{-1})	g_{total}	Energy (cm^{-1})	g_{total}
0.	1	0.	4
93450.	8	1432.	2
95000.	4	108722	2
104100.	3	132500.	20
105500.	12	135000.	12
106100.	8	139000.	6
107900.	13	157000.	20
111750.	4		
113600.	23		
116200.	15		
119250.	48		

Ar III (I.P.= 329383. cm^{-1})		Ar IV (I.P.= 481512. cm^{-1})	
Energy (cm^{-1})	g_{total}	Energy (cm^{-1})	g_{total}
0.	5	0.	4
14010.	5	21000.	10
33270.	1	34000.	6
115000.	9	117000.	12
144000.	3	145000.	10
187000.	29		

Table II-3 (cont.)

Ar V

(I.P.= 604004. cm^{-1})

Energy (cm^{-1})	g$_{total}$
0.	1
16300.	5
121000.	15
141000.	9

Ref.: C.E. Moore Atomic Energy Levels, Vol. I, National Bureau of Standards, NSRDS-NBS 35, 1971.

Table II-4

Lennard-Jones Parameters for Calculation of Collision Cross Sections

Collision Partners	Lennard-Jones Parameter (A)
A - A	3.44
A - H	2.7
A - H_2	3.2
H_2 - H_2	2.97
H_2 - H	2.6
H - H	2.0

Ref.: J.O. Hirschfelder, C.F. Curtiss, and R.Byron Bird, Molecular Theory of Gases and Liquids, Wiley, New York, 1954.
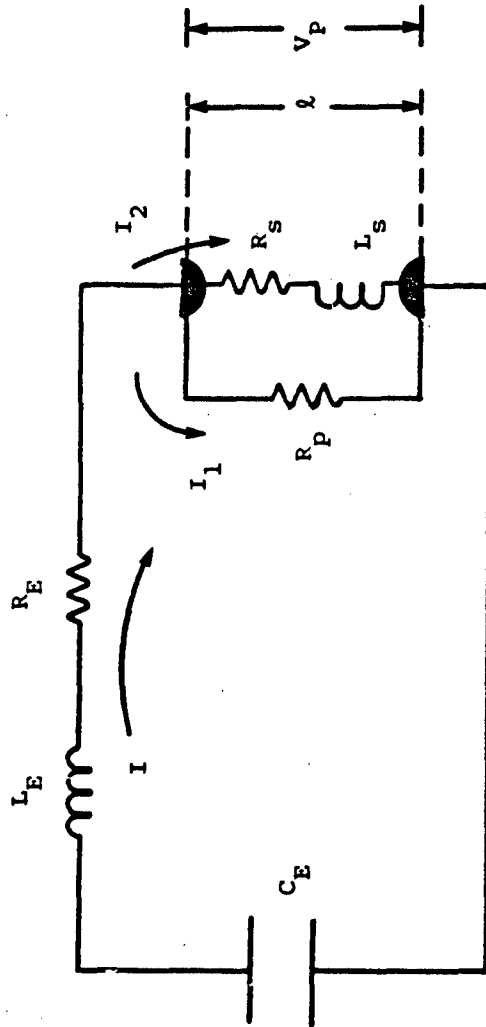
Figure II-1. Schematic of External Electrical Circuit.

References for Section II

II.1) M. Mitchner and C.H. Kruger, <u>Partially Ionized Gaes</u> (New York: Wiley Interscience) 1973.

II.2) C.L. Longmire, <u>Elementary Plasma Physics</u>(New York: Wiley Interscience) 1967.

II.3) L. Spitzer, Jr.,<u>Physics of Fully Ionized Plasmas</u>(New York: Wiley Interscience) 1967.

II.4) I.S. Marshak,ed., <u>Pulsed Light Sources</u>,(Energy Press, Moscow) 1978. (Lawrence Livermore National Laboratory Translation 02974 ,AD-EX Job No. 56678)

II.5) D.R. Stull and H. Prophet,<u>JANAF Thermochemical Tables, Second Edition</u>, (Nat. Bureau of Standards NSRDS-NBS 37, Washington D.C.) 1971.

SECTION III

SIMULATED SPARK COLUMN CHARACTERISTICS

In this section, simulated densities, temperatures, and circuit quantities for a spark column in a mixture of Xe/H_2:0.01/0.99 will be examined. The initial gas pressure is 2 atm and the charging potential is 40 kV. The electrodes are separated by 1.2 cm and the current return path is 14 cm in diameter. The external inductance is 20 nH. The on axis preionization electron density is 10^{14} cm^{-3} and has a radius of 50 μm. The duration of the preionization pulse is assumed to be very short so that the initial electron density appears instantaneously. The intent of this exercise is to illustrate the canonical characteristics of a laser triggered spark column. The general trends discussed here apply to a wide range of initial conditions and gas mixtures; the details, of course, change.

III.A. Hydrodynamic Quantities

The density of heavy particles, in units of $\Delta\rho/\rho_o$ are is plotted in Fig. III-1a. The initial density is 2.7×10^{-4} g/cm^3. The same data is plotted in Fig. III-1b in absolute units. The pressure and and gas temperature fields for the same conditions are plotted in Figs. III-2, and III-3 respectively. The velocity field is plotted in Fig. III-4. The radial pressure gradient is the accelerating force for the convective velocity. The magnitude of the accelerating force is proportional to the density of contours in the horizontal direction of Fig. III-2. The gas remains nearly motionless during the first 10 ns as this is the time required for the electron density to avalanche to a sufficiently large value to begin heating the heavy particles. Concurrent with the increase in gas temperature (Fig. III-3) the gas pressure begins to increase, first near the axis and later at points at larger radii. The maximum pressure within the arc is approximately 600 atm. The subsequent pressure gradient initiates convective motion of the gas (Fig. III-4).

Convection, and subsequent expansion of the ionized core of the spark, begins as the gas within the core is heated by electron impact collisions. Although numerous and hot, the pressure of the electron fluid contributes to the pressure gradient only in the ratio of the ion mass to the total heavy particle mass. This is a consequence of the conditions of ambipolar diffusion. (See Section II. C.) As the hot gas begins to convect radially outward, a low density core is left behind and a region of

III-1

increased heavy particle density begins to form at the edge of the ionized region. (See Fig. III-1) Although cold, the pressure of this high density gas increases to the point that it too begins to convect. At this point, a shock begins to form. The shock is initially strong ($\Delta\rho/\rho_0 > 5$) and thin (width < 5 μm), and later weak ($\Delta\rho/\rho_0 \approx 5$) and thick (width > 30 μm). The mass density of the hot core is reduced to a value < 0.05 that of its initial value, and the core is nearly isothermal. The inner contour in Fig. III-3 corresponds to a temperature of 50,000 K. The temperature gradient between this high value and its ambient value occurs across a thin region of gas just interior to the shock and penetrates into the shock for approximately half its width. These conditions impact heavily on the distribution of atomic and molecular species in the plasma column. (See Sec. III. B.)

After the first 20 ns of convection, the pressure gradient within the core decreases leaving nearly isobaric conditions. As the arc continues to expand, pressure in the isobaric core slowly decreases. Steep pressure gradients are delegated to the outer regions of the arc. The transition between the core (pressures of many hundreds of atmospheres) and the cool gas exterior to the core (pressure of a few atmospheres) occurs across the shock that has a thickness of only tens of microns. The location of the maximum velocity is just interior to the shock front. At a particular radial location, the convective velocity monotonically increases to its maximum value. Although remaining positive, as the convective velocity decreases from its maximum value it may oscillate, responding to small changes in the pressure gradient. These pressure and velocity oscillations result in oscillations in the height of the shock front (Fig. III-1), the amplitude of which damps in time.

Convection is the spark column's attempt to reduce a pressure gradient The convective velocity continues to increase until the pressure gradient is reduced to a low value as a result of the redistribution of mass by convection. The direction of the convective velocity can reverse with a sufficiently large change in the sign of the pressure gradient. This is an effect which is commonly seen in bounded systems, such as an arc sustained within a discharge tube where convection will cause mass to accumulate at the wall thereby increasing the gas pressure at that location. In our system, though, the walls are sufficiently far away that expansion of the spark column during the first 100 ns is not hindered by significant reversals in the pressure gradient. Any reversal in the pressure gradient is not large enough in magnitude or long enough in duration to reverse the convective velocity. Under certain conditions,

though, significant reversal of the pressure gradient can occur. These
conditions will be discussed below in Sec. V.B.

The shell of high neutral particle density serves two nearly opposing
functions; to both limit the rate of growth of the column and to provide
the seed electrons required for an avalanche the gas, thereby expanding the
gas by non-convective means. The accumulation of mass in the shock front
increases the pressure gradient required to accelerate that mass to a given
velocity. The high density shell also presents a region with a low E/N
which inhibits the electrons from avalanching. In these respects, the high
density shell confines the arc. The high density shell serves as a source
of seed electrons by trapping ionizing radiation from the core and by
thermal ionization resulting from its adiabatic compression. The fact that
the photoionization occurs in a region of low E/N is unfortunate as the
probability for avalanche is low. The use of additives having an
ionization potential below that of hydrogen and xenon, and therefore can be
ionized by radiation to which the shock front is transparent is a method to
increase the rate of arc expansion.

III.B. Atomic and Molecular Densities: Ion and Neutral

Electron density for the spark column examined in the previous
section is plotted in Fig. III-5. The contours span the range from 2 x
10^{19} to 1 x 10^{18}. To an accuracy of a few percent (see below) this
Fig. III-5 is also a plot of the of the density of H^{+}. The electron
density reaches its maximum value near the axis and early during the
discharge pulse before the heavy particle density has been depleted by
convection. The maximum electron density does not correspond to the
maximum in fraction ionized. As the gas convects, thereby lowering the
mass density in the core, the electron density decreases by a smaller
fraction than the mass density thereby increasing the ionized fraction.
After 35 ns, the core is fully ionized. For gas mixtures that are greater
than 95% hydrogen, the electron temperature in the core exceeds 15 eV.
This elevated temperature results from the fact that after the molecular
hydrogen has been dissociated and the atomic hydrogen ionized, there is not
a significant density of species remaining with which electrons can have
inelastic collisions. The only remaining energy loss mechanisms for
electrons in the core at this time are elastic collisions with ions or
bremsthrallung, neither of which are efficient dissipators of energy.
Cooling of the electrons occurs as the core expands, lowering the impedance
of the discharge and the resulting E/N.

The densities of Xe^+ and Xe^{++} (the highest ionization state considered for this calculation) are plotted in Fig. III-6. Xe I has the lowest ionization potential of all the species in the mixture and therefore is the first to be ionized. At the high electron temperature afforded by the high fraction of H_2, Xe I is rapidly ionized to create a region where all xenon species are Xe II, which in turn are ionized to leave a core where virtually all xenon is Xe III.

Although initially the most abundant neutral species, H_2 is also a highly volatile species in the hot spark column environment. The dissociation potential of H_2 is 4.5 eV and that of H_2^+ is 3.4 eV. Dissociation proceeds by electron impact collisions and by thermal dissociation, requiring only moderate heating of the gas ($>$ 5000 K) to result in significant dissociation. The additional mechansim of dissociative recombination is also available to the ion. Once the molecular species are dissociated a major electron energy loss mechanism, that of vibrational excitation is eliminated, thereby enabling the electron temperature to climb to a higher value. The higher local electron temperature leads to rapid and ultimately total ionization. This sequence of events is illustrated in Fig. III-7 where there are plots of the densities of H_2, H_2^+, and H. At early times, before the gas has significantly heated or avalanched, molecular hydrogen is only slowly depleted near the axis. After about 20 ns, molecular hydrogen begins to first ionize and then dissociate. To the left of the low density contour, H_2 is fully dissociated. The density of H_2 is high in the shock wave, however the width of the region in which H_2 is at high density is narrower than that of the shock. (See Fig. III-1b.) This indicates that H_2 is thermally dissociating on the inner side of the shock and being replaced by atomic hydrogen. (See Fig. III-7b.)

After the first 30 ns, atomic hydrogen exists only within and just interior to the shock. It is in this region where the gas is hot enough to fully dissociate H_2 however the electron density is not yet high enough to deplete, by ionization, the atomic hydrogen. The density of H_2^+ proceeds through a similar, but even more volatile sequence. (See. Fig. III-7c.) Early in the discharge, H_2^+ is the most abundant ion. As the gas heats and the electron density increases, H_2^+ is rapidly dissociated. The region in which the rate of ionization of H_2 exceeds the rate of dissociation and recombination of H_2^+ is confined to a very narrow portion of the shock.

(b)

CONTOUR VALUES $\times 10^{-4}$ g/cm³

(a)
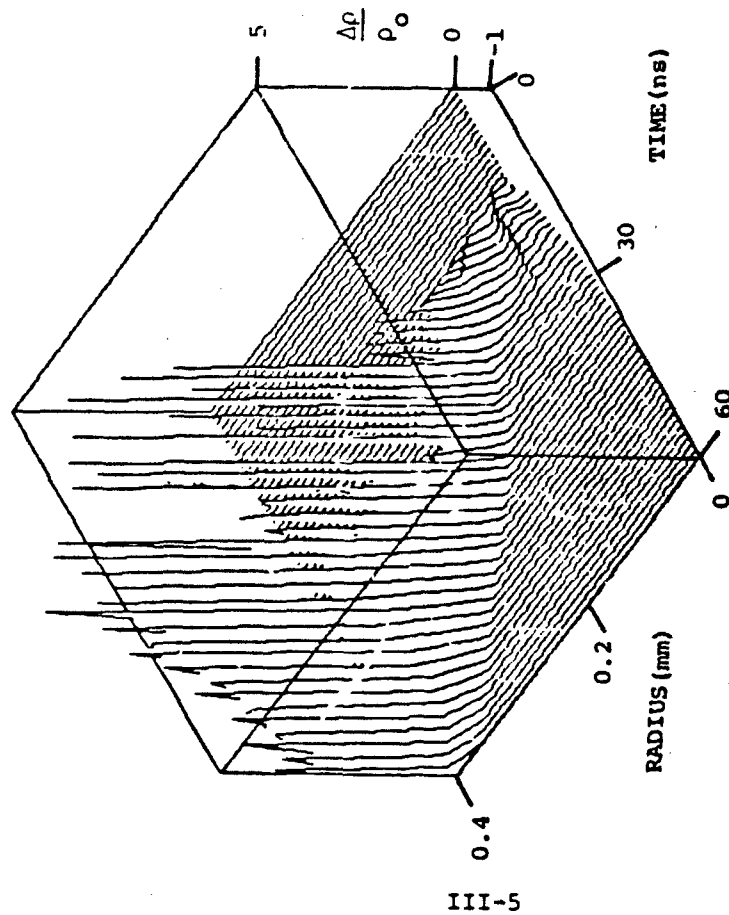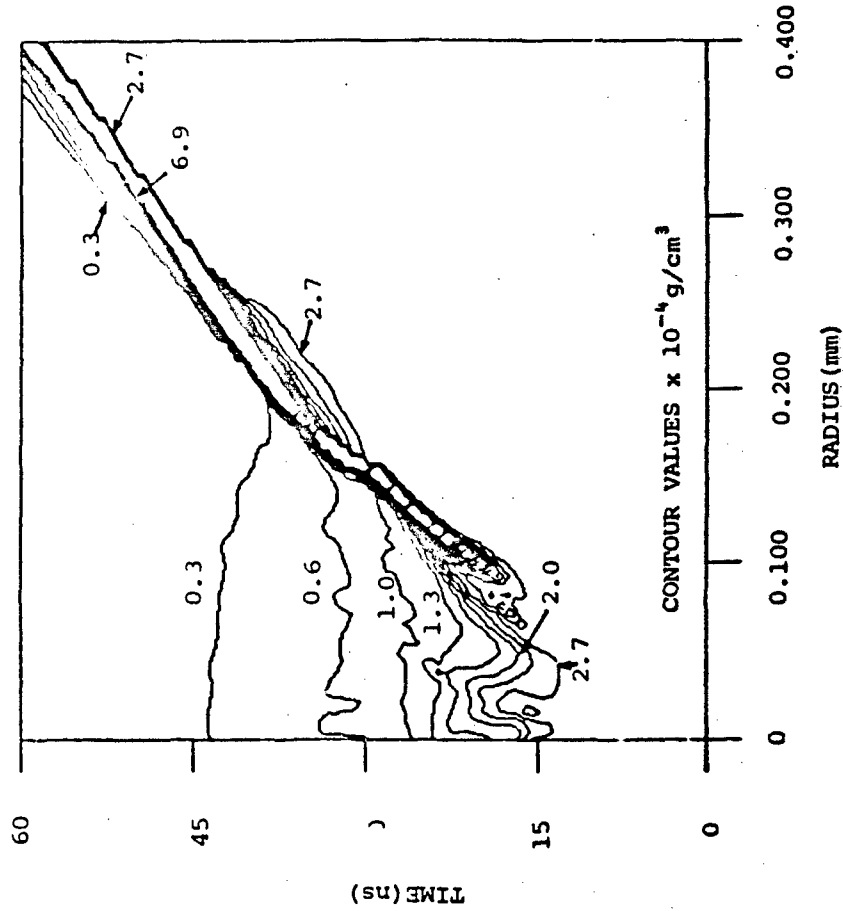
Figure III-1 Typical Mass Density for Spark Column in a Xe/H_2:0.01/0.99 Gas Mixture. Both figures are of the same data. (a) $\Delta\rho/\rho_o$; (b) absolute mass density.
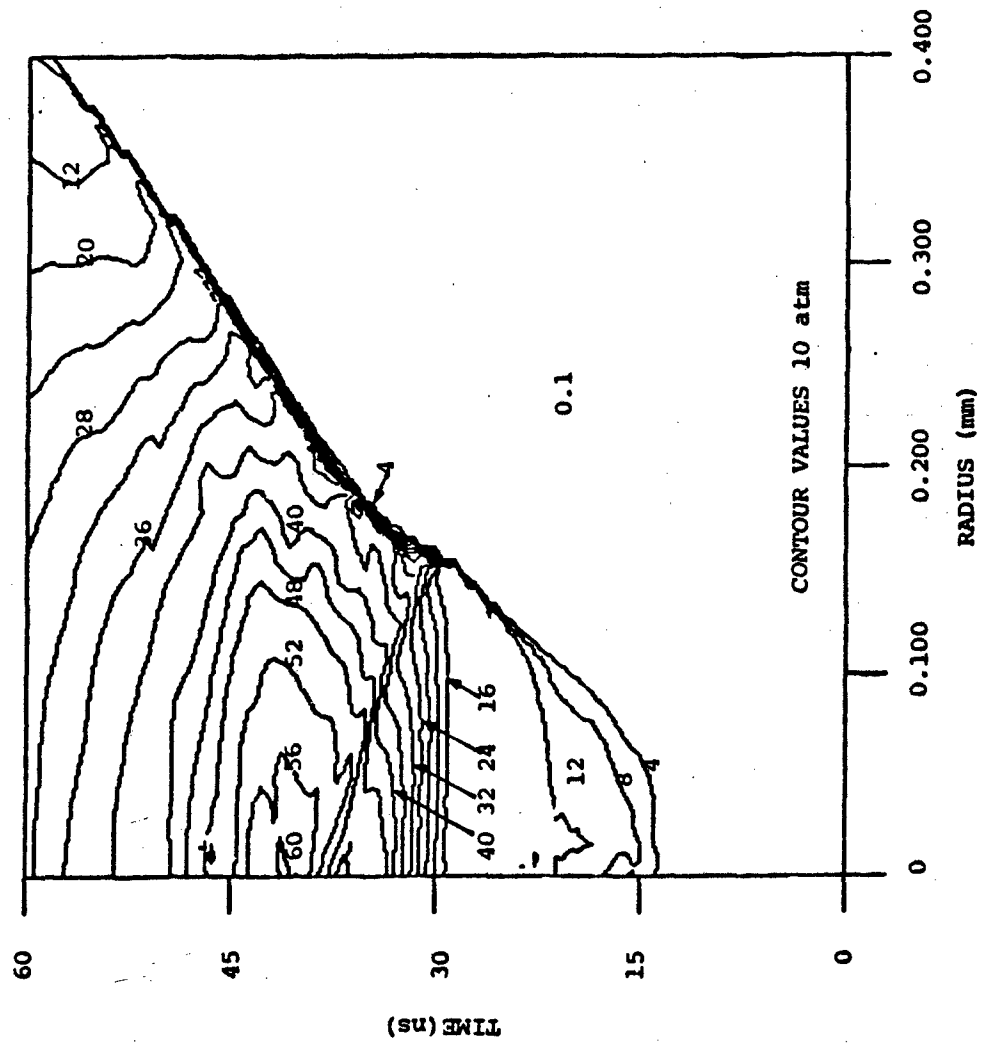
Figure III-2 Thermodynamic Pressure for a Spark Column in a Xe/H_2:0.01/0.99 Gas Mixture

CONTOUR VALUES 10 atm

RADIUS (mm)

TIME (ns)
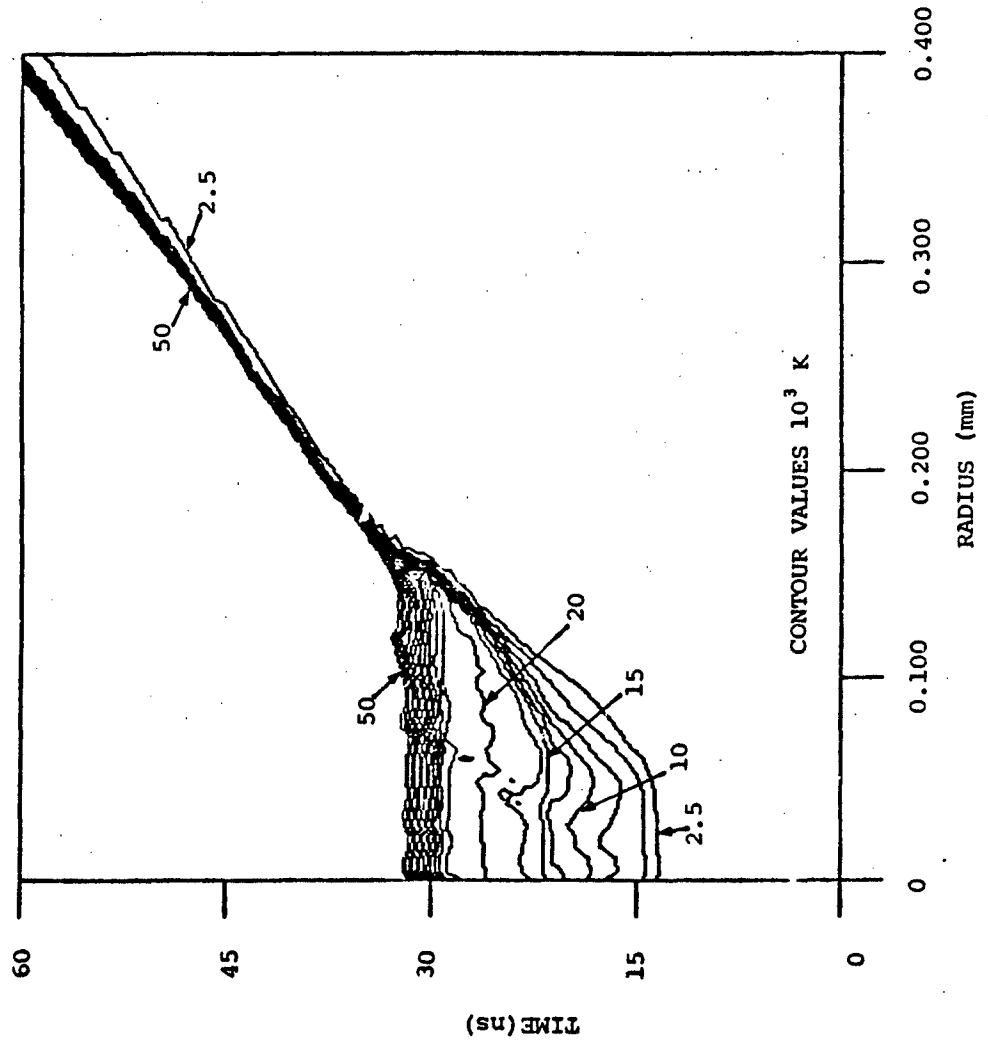
Figure III-3 Heavy Particle Temperature for a Spark Column
in a Xe/H_2:0.01/0.99 Gas Mixture
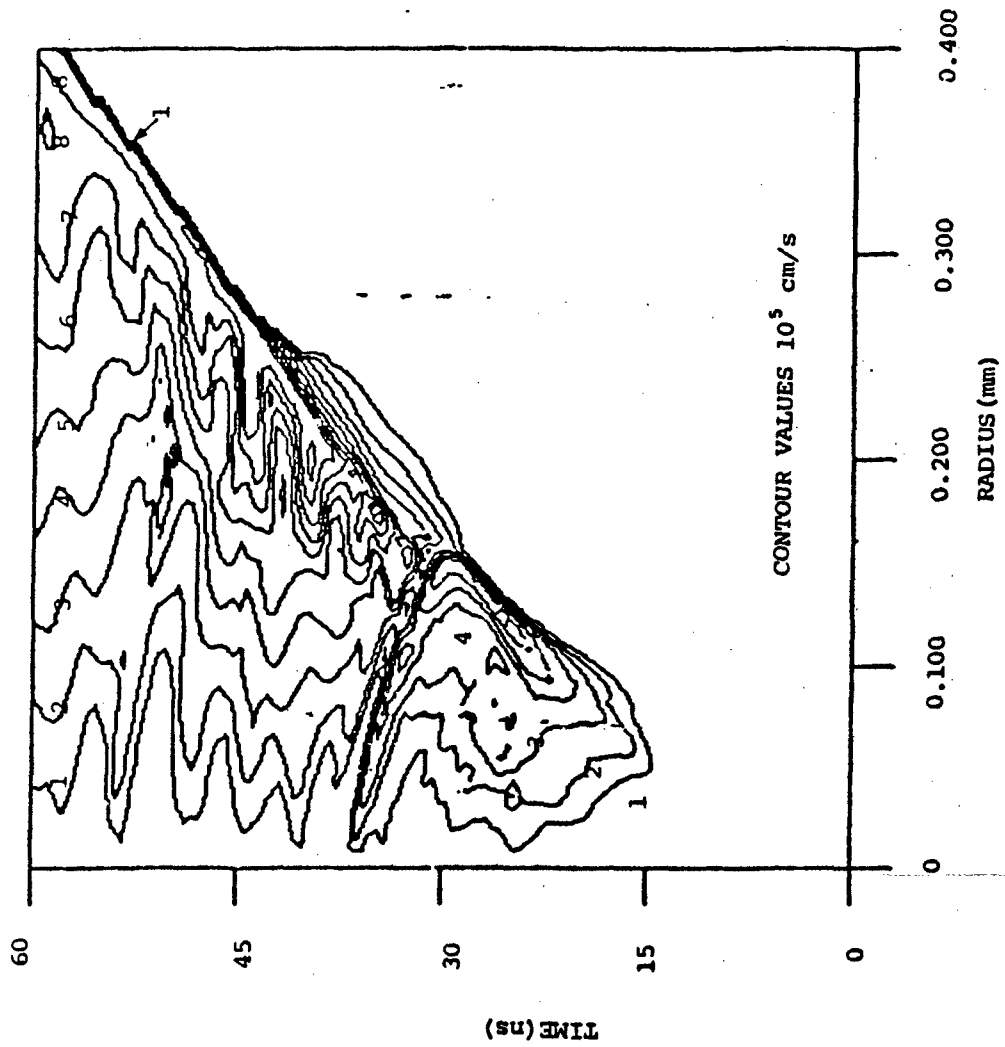
Figure III-4 Velocity Field for a Spark Column in
a Xe/H_2:0.01/0.99 Gas Mixture
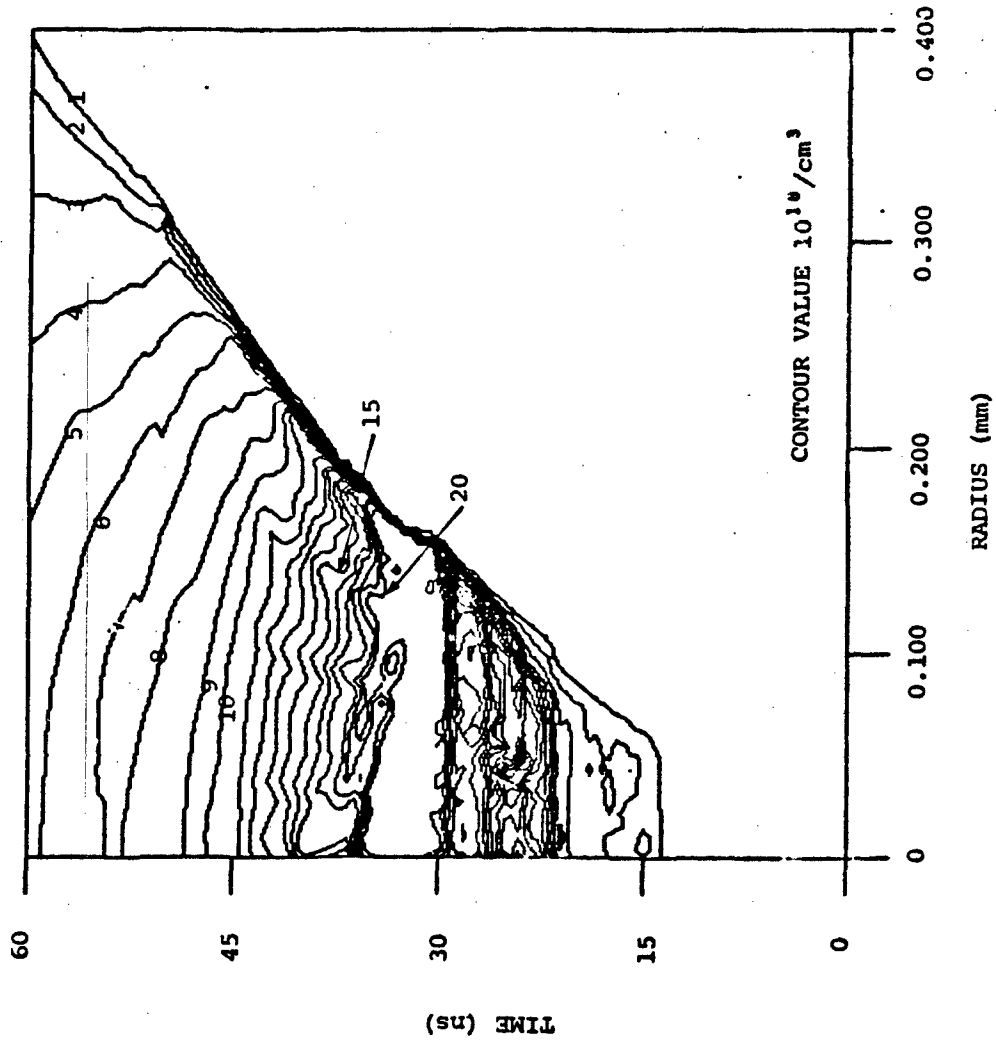
Figure III-5   Electron Density for a Spark Column in a
Xe/H$_2$:0.01/0.99 Gas Mixture

III-9
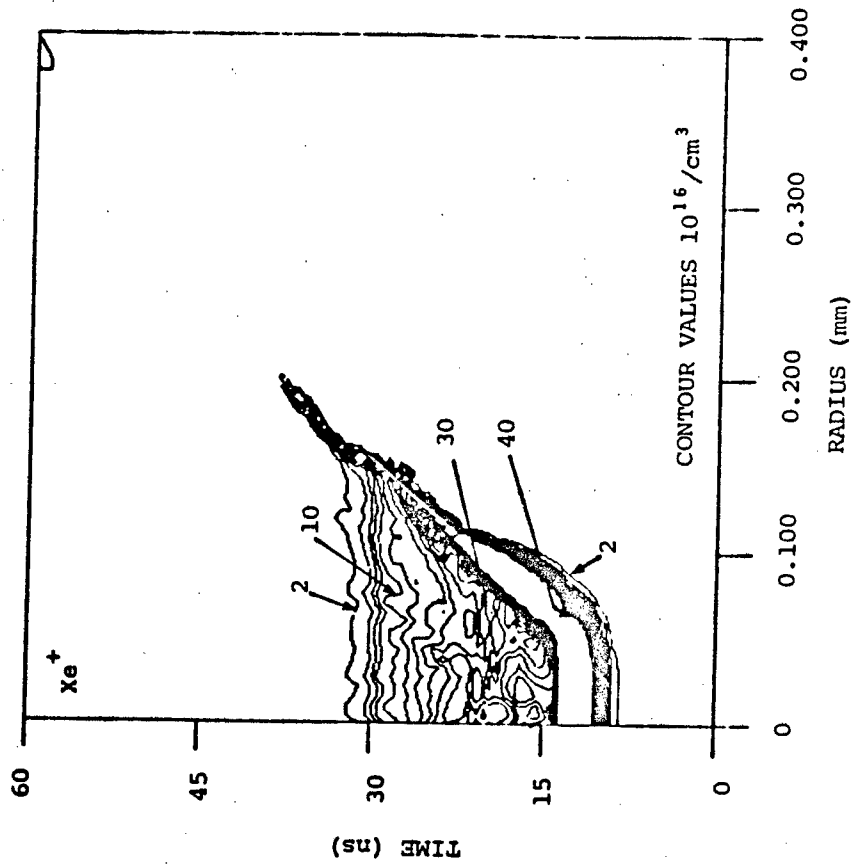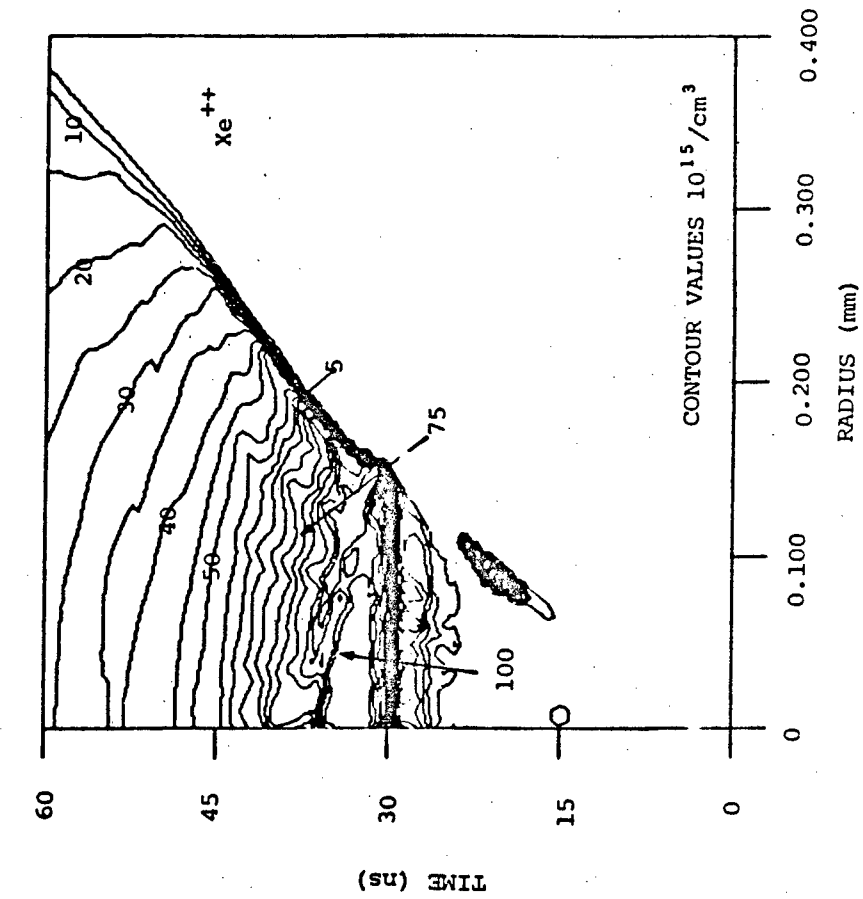
Figure III-6 Density of Ionized Xenon for a Spark Column in a Xe/H_2:0.01/0.99 Gas Mixture. (a) Xe^+; (b) Xe^{++}
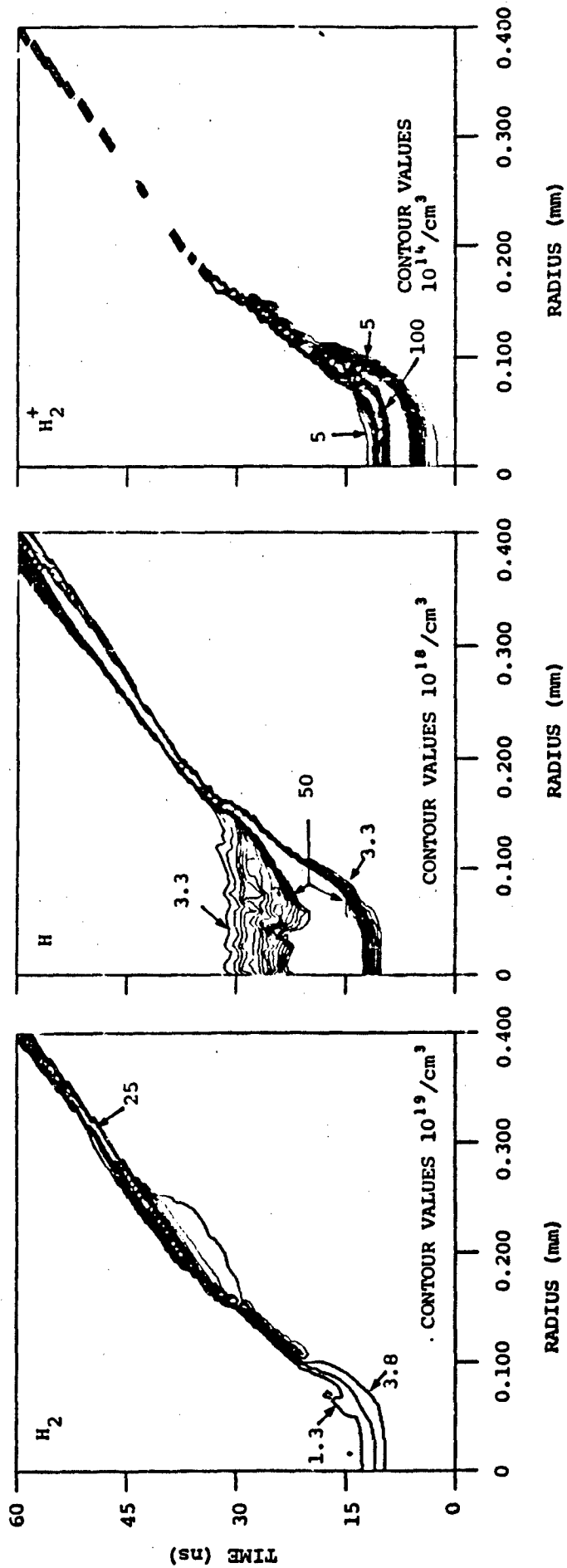
Figure III-7   Density of Hydrogen Species for a Spark Column in a Xe/H$_2$:0.01/0.99 Gas Mixture.   (a) H$_2$; (b) H; (c) H$_2^+$.

SECTION IV

RATE OF ARC FORMATION AND EXPANSION

In this section, the rate of arc formation and expansion will be examined for various initial conditions including preionization electron density, charging voltage, and gas composition.

IV.A. Delay Time for Voltage Collapse

There are two time quantities of interest in laser triggering of spark gaps. The first is delay time, the time between the laser induced breakdown and voltage collapse of (or current flow through) the gap. The second quantitity of interest is jitter, the scatter in delay time for a given laser intensity for a large number of trials. The former quantitity, delay time, was examined with the model as a function of initial electron density. These results are plotted in Fig. IV-1. The delay time for this figure is defined as the time between laser triggering, that is the time at which the preionization laser instanteously produces the indicated electron density, and when the current reaches a value of 100 A. Clearly, the delay time decreases with increasing initial electron density. True avalancning, and hence current flow, does not occur until multistep ionization becomes a significant fraction of the total rate of ionization. The final characteristics of the spark column are relatively independent of the initial electron density. Obtaining a given value of current or electron density is merely shifted in time by a value equal to the delay time.

To compare the computed values for delay time with experimental measurements,[IV.1] an assumption must be made as to the laser ionization process. The ionization potential of the neutral gas is 12.5 eV for Xe (mole fraction .01) and 15.5 eV for H_2 (mole fraction 0.99). The energy of the laser photon is ~ 4.4 eV Therefore, a minimum of 3 photons are required to ionize the Xe and 4 photons are required to ionize the H_2. If we assume the ionization to be a 4-photon process, then the initial electron density, n_{e0}, is proportional to I^2, where I is the intensity of laser used for preionization. Using this assumption, and normalizing an initial electron density of 10^{14} cm^{-3} to an intensity of 10^8 W/cm^2, experimental points are also plotted in Fig. IV-1. The agreement is very good indicating that the ionization process may indeed be by 4-photons.

IV.B. Effect of Molecular Weight

Recall that the sound speed of a gas at temperature T and of average molecular weight M is[IV.2]

$$c_s = \left[\frac{\gamma kT}{M}\right]^{1/2} \qquad\qquad\qquad [IV-1]$$

Providing that the dominant expansion mechanism for our arc columns is a hydrodynamic sonic expansion of the hot plasma, the expansion rate can be effected by a change in plasma temperature or in molecular weight of the gas. Arc radius (defined as the outer radius at which the electron density falls to .05 of the instantaneous maximum value) as a function of time for three different Ar/H_2 gas mixtures are plotted in Fig. IV-2 to illustrate this effect. As the average molecular weight of the mixture increases, and the average sound speed decreases, the rate of arc expansion decreases. Note, though, that for the first forty nanoseconds, which includes the time delay discussed above, the rate of expansion for all cases is nearly identical. Although the heavy particles within the core are hot ($T_g >$ 15000 K) there has been insufficient time for the pressure gradient to acclerate the particles to a significant velocity. During this period, radiation transport and subsequent photoionization of the neutral gas outside the plasma column is responsible for expansion of the arc. As the gas accelerates, convection becomes the dominant expansion mechanism. At this time, the expansion rate for plasmas with different molecular weights begins to diverge. The gas mixture with the lower average molecular weight, and corresponding high sound speed, expands at the higher rate.

IV.C. Recombination as a Plasma Heating Mechanism

Collisional radiative recombination is believed to be the dominant recombination mechanism for the arcs of interest. The rate coefficinet for this process is inversely proportional to the 9/2 power of the electron temperature.[IV.3] Therefore in hot plasmas (many electron volts), the recombination rate coefficient is small. The total rate of recombination, though, is proportional to the cube of the electron density. Therefore even in hot plasmas with large electron densities, the total rate of recombination can be large. In a collisional radiative recombination, a portion of the kinetic and potential energy of the recombining electron is carried off by the electron that is its collision partner. This energy remains in the electron gas. The total electron density, though, is reduced by one electron. The result is that the total average energy of the electron distribution increases. This process is known as recombination heating and is a mechanism by which a significant amount of

energy is retained in the gas. Recombination is not an external source of energy, as is joule heating. Rather, recombination heating is a mechanism whereby the energy of the recombining electron is distributed to the remaining electrons. This energy is originally put into the system by external means and is stored in the kinetic and potential energy of the recombining electron. Had the recombination been purely radiative instead of collisional radiative, then the energy of the recombining electron could only be recovered if the resulting photon is absorbed by the plasma.

The rate of recombination heating, R_r, is given by

$$R_r = \left[\frac{3}{2}kT_e + (1-f)\epsilon_I\right] \frac{r_r n_e^3}{T_e^{9/2}} \tag{IV-2}$$

where the ϵ_I is the ionization potential of the state into which the electron recombines and f is the fraction of that energy that is radiated away during the recombination. The first term of Eq. IV-2 is for the thermal (kinetic) energy of the recombining electron and the second term is for the potential energy of the recombining electron. For typical values in our plasma ($j = 3$ MA/cm^2, $\sigma = 100$ Ω-cm) the rate of joule heating is 90 GW/cm^3. The rate of recombination heating ($T_e = 4$ eV, $\epsilon_i = 5$ eV, $n_e = 10^{19}$) is approximately 15 GW/cm^3, and is an appreciable fraction of the total energy input. Energy by this process can have a siginificant impact on the arc dynamics.

The degree to which recombination heating is important in the expansion of the arc was investigated with the model, the results of which are plotted in Fig. IV-3a. Arc radius is plotted as a function of time for two case which differ only in the inclusion or absence of recombination heating (Eq. IV-2). The arcs are for mixtures of Ar/H2:0.2/0.8. Electron temperature for the same conditions at 30 ns after triggering is plotted in Fig. IV-3b. The rate of arc expansion is faster for the case with recombination heating, though only marginally so. The electron temperature for this case is only about 10% higher near the axis however it is siginifcantly higher towards the edge of the spark column. (Note the decrease in electron temperature in high density region where E/N is low.)

Small perturbations in the temperature of the plasma, as plotted in Fig. IV-3b, can cause significant changes in the properties of the plasma, especially electron density. Recall that the rate of ionization scales as $\exp(-\epsilon_I/T_e)$, where ϵ_I is the ionization potential, while collisional

IV-3

radiative recombination scales as $T_e^{-9/2}$. Therefore a small increase in the electron temperature not only increases the rate of ionization but also decreases the rate of recombination. Using these simple scaling laws, one can show that

$$\frac{\Delta n_e}{n_e} \approx \frac{\Delta T_e}{T_e} \left[\frac{\epsilon_I}{2T_e} + 1 \right] \qquad \text{[IV-3]}$$

Electron density for the two cases discussed above is plotted in Fig. IV-4 as a function of radius approximately 30 ns after triggering the spark column. The case with recombination heating has an average electron density about twice that of the case without recombination heating, and also shows more "shell structure" than the case without heating. This region of high electron density corresponds to the region of higher electron temperature in Fig. IV-3b. (Note that both cases also show a penetration of the plasma into the high density shock wave, a result of local sources of photo- and thermal- ionization.)

IV.D. Arc Expansion as a Function of Charging Voltage

The rate of arc expansion can be expected to be a function of both the magnitude of energy deposited in the plasma and the rate of deposition. Computed mass density and arc radii for spark columns having different values of charging voltage are plotted in Fig. IV-5. As one would expect, the rate of arc expansion increases with increasing charging voltage. Note other qualitative trends in the plots of mass density as charging voltage, and hence rate of energy deposition increaes. The thickness of the shock decreases and its height (in terms of $\Delta\rho/\rho_o$) increases with increasing charging voltage, while the local minimum in shock height occurs at progressively earlier times with this increase. The average mass density within the core of the spark also increases as charging voltage increases. This trend indicates local reversals in the pressure gradient resulting from rapid heating of the interior of the shock. Reversal of the pressure gradient can slow, or reverse, the radially outward directed convection.
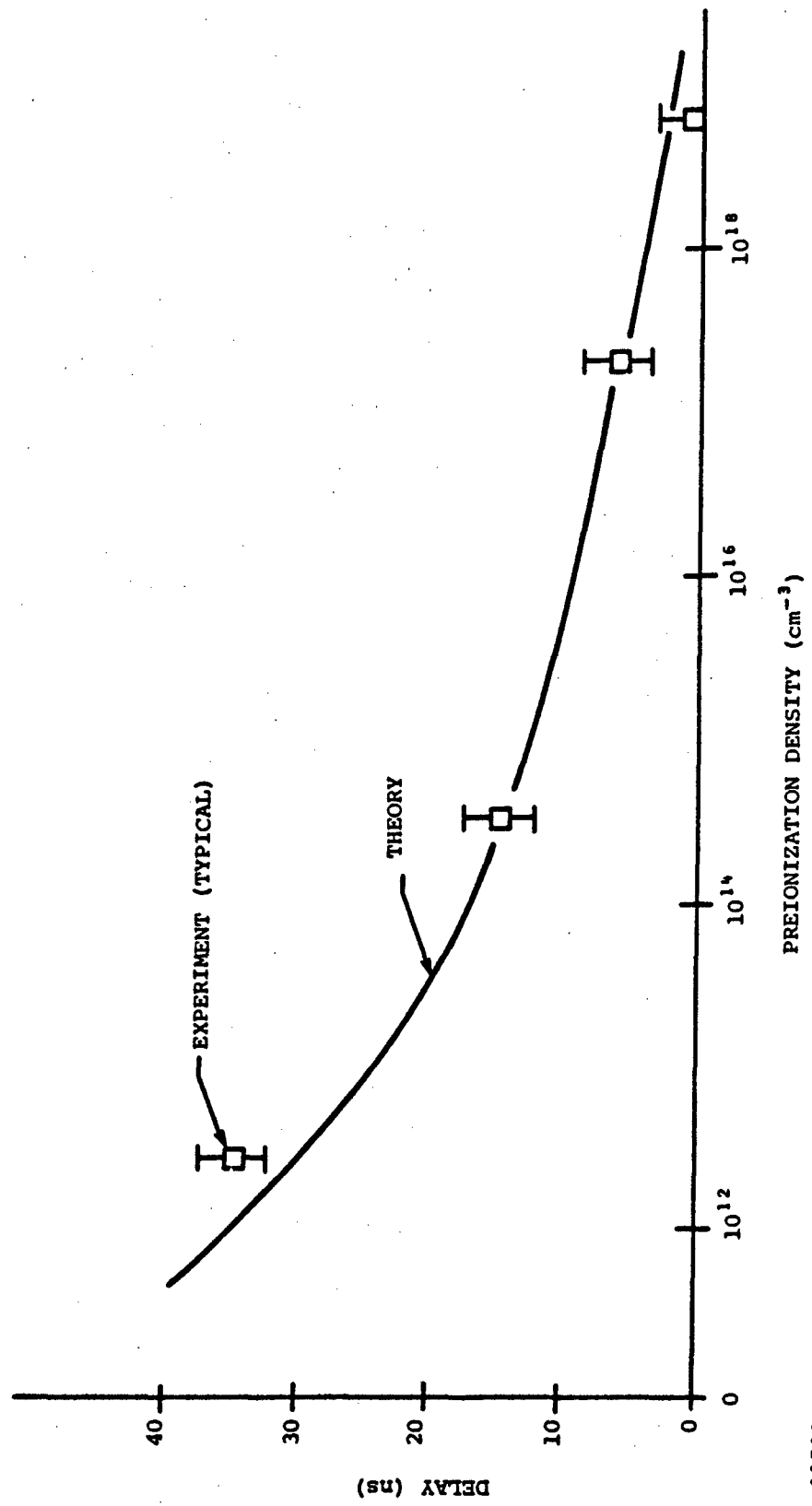
Figure IV-1. Computed and Experimental Delay Times Between Laser Triggering and Voltage Collapse as a Function
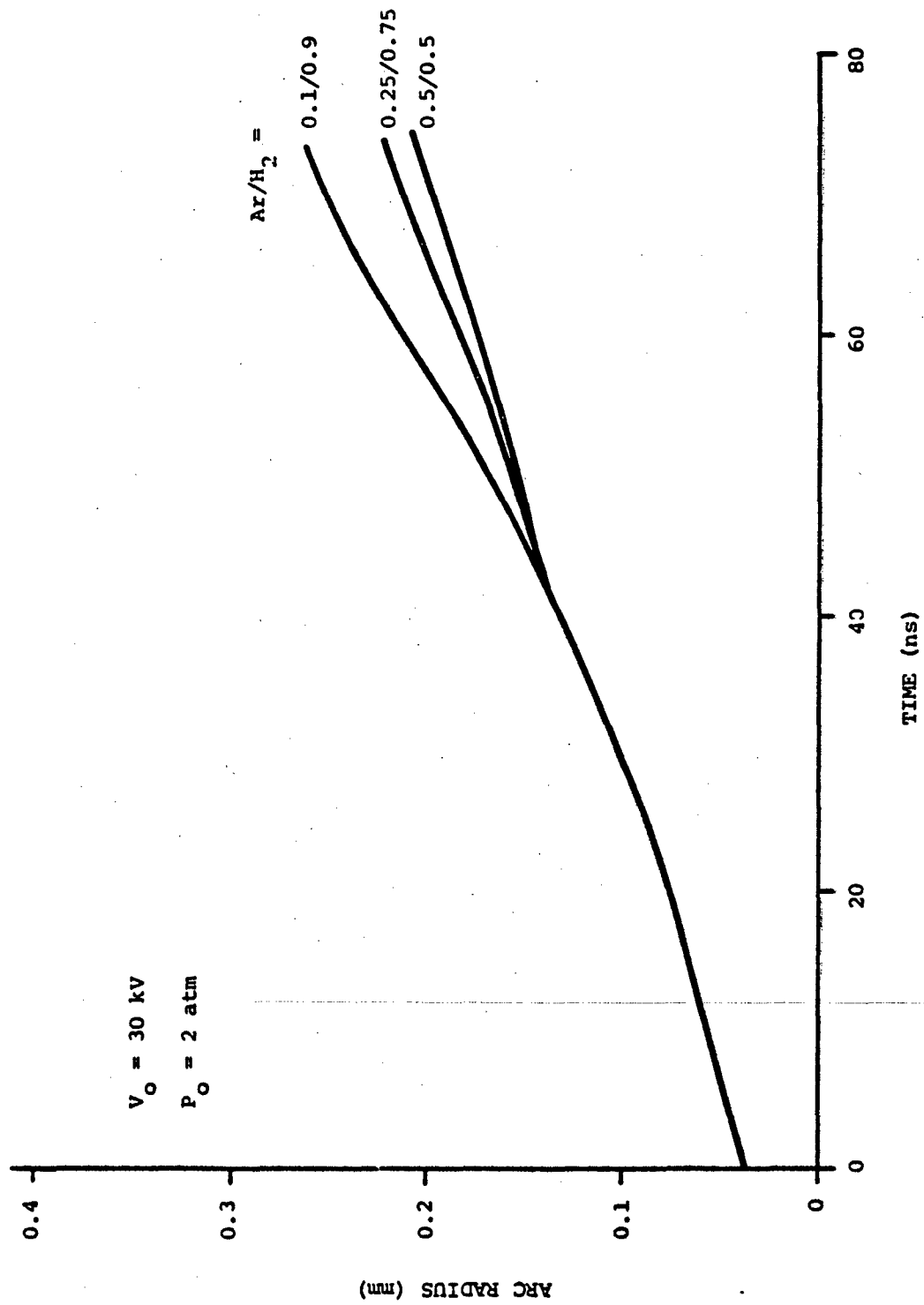
Figure IV-2. Arc Radius as a Function of Time for Different Molecular Weights and Mixtures of Ar/H$_2$.

84 08741
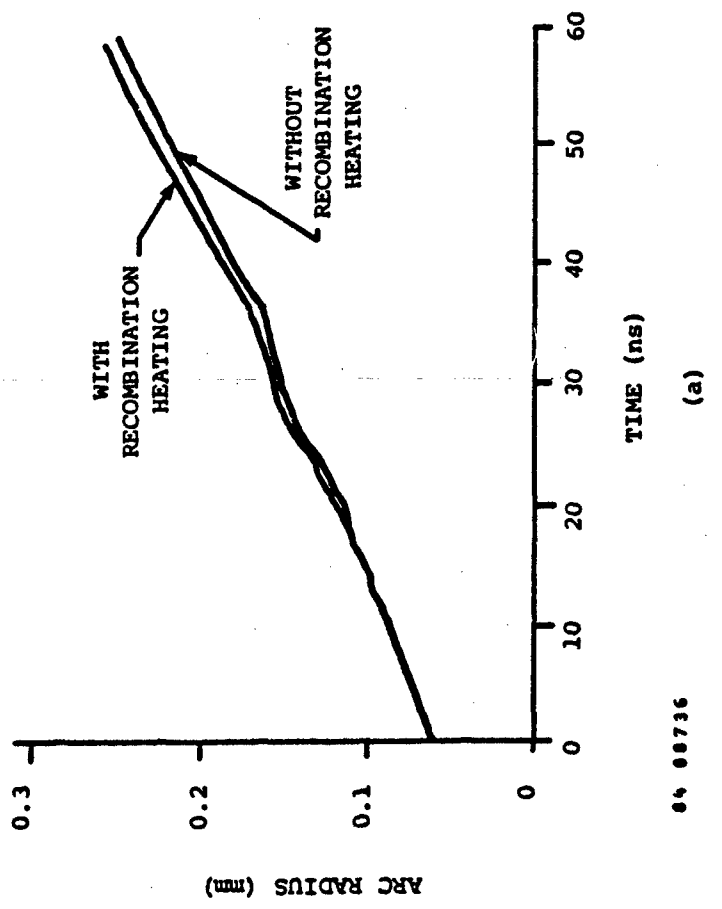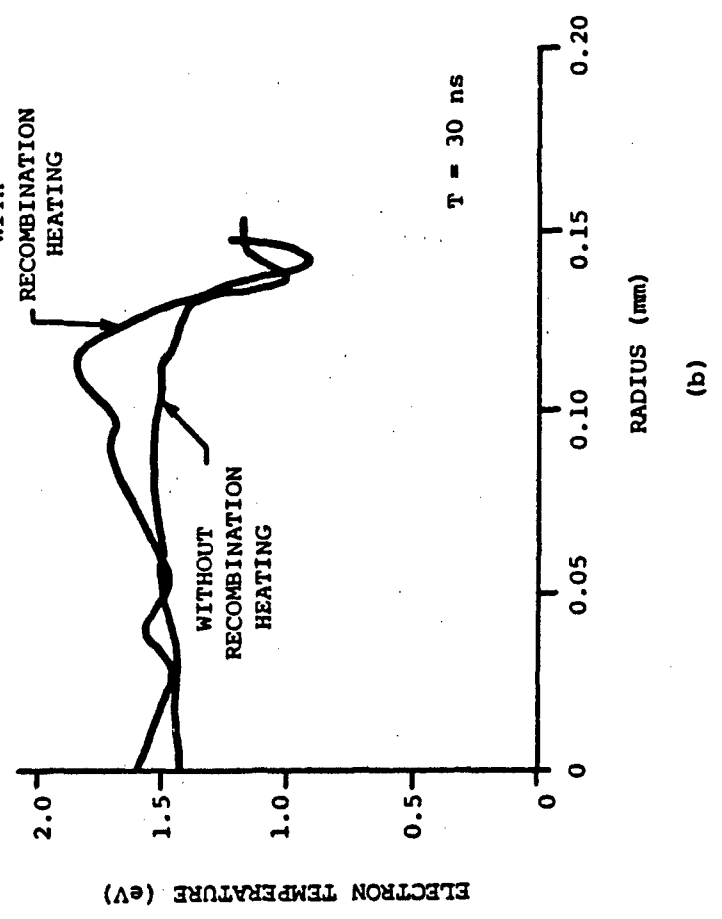
IV-6

Figure IV-3. Conditions With and Without Recombination Heating.
(a) Arc radius; (b) electron temperature.

8. 08736

IV-7
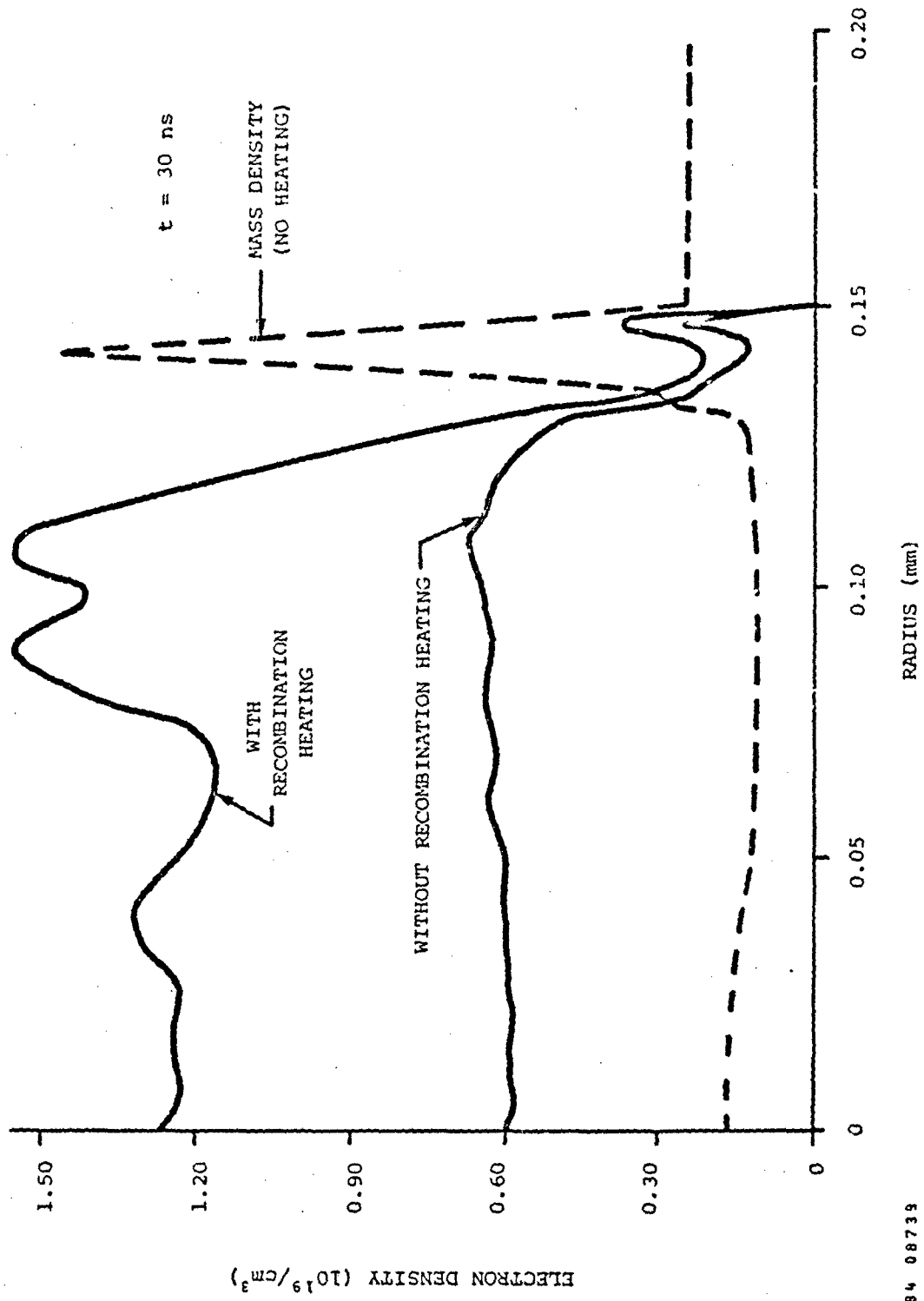
Figure IV-4. Electron Density With and Without Recombination Heating.

t = 30 ns

MASS DENSITY
(NO HEATING)

WITH
RECOMBINATION
HEATING

WITHOUT RECOMBINATION HEATING

RADIUS (mm)

ELECTRON DENSITY ($10^{19}/cm^3$)

84 08739

IV-8
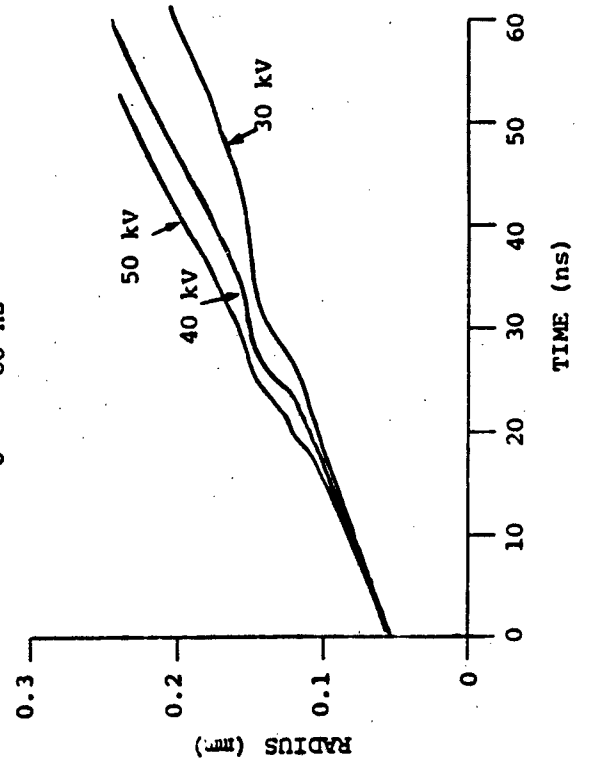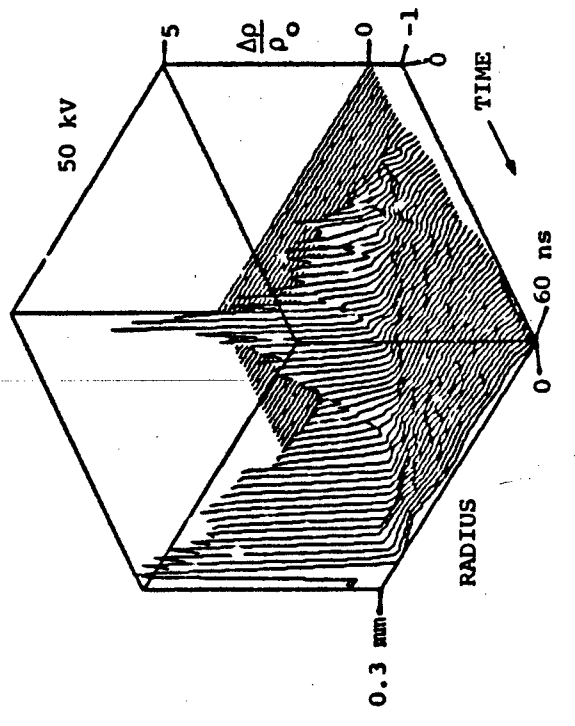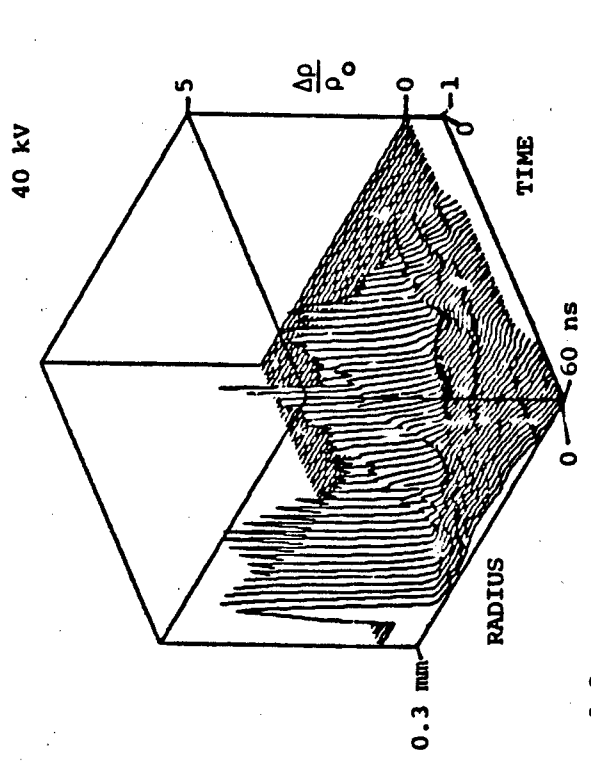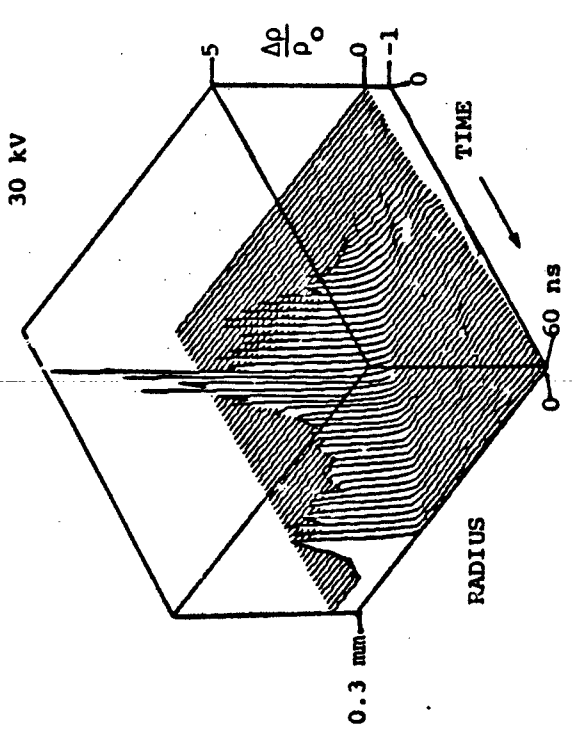
Figure IV-5 Mass Density ($\Delta\rho/\rho_o$) and Arc Radius for Spark

References for Section IV

IV.1) Experimental data obtained under contract to Naval Surface Weapons Center Contract No. N60921-83-C-A057.

IV.2) P. A. Thompson, <u>Compressible-Fluid Dynamics</u> (New York: McGraw-Hill) 1972.

IV.3) M.A. Biondi, "Recombination", in <u>Principles of Laser Plasmas</u>, G. Bekifi, ed. (New York: Wiley Interscience) 1976.

INVERSION OF COMPUTED DATA TO SIMULATE INTERFEROGRAMS
AND COMPARISON WITH EXPERIMENTAL DATA.

V.A. Introduction

Experimentally obtained interferograms of laser triggered spark
columns record the product of the change in index of refraction from the
ambient value with the path length. This product can be related to the
local electron density and the change in heavy particle density. The
measured values are line of sight (LOS) data. In order to obtain data as a
function of radial position within the column, an Abell inversion must be
performed. For LOS data recorded as a function of the transverse
coordinate x, F(x), the corresponding radial function, G(r) is obtained by
performing the integral[V.1]

$$G(r) = -\frac{1}{\pi} \int_r^R \frac{\left[\frac{dF(x)}{dx}\right]}{\left[y^2 - r^2\right]^{1/2}} \, dy \qquad [V-1]$$

where R is the radius of the cylinder of interest. For our purposes, the
function F(x) is the fringe shift of the probing laser resulting from
changes in heavy particle density or electrons. In order to separate the
contributions of electrons and heavy particles in the inteferograms, and
hence obtain their densities, inteferograms at two different wavelengths
must be inspected, and their inverted profiles subtracted. In principle,
this is a straight forward exercise. In practice, though, local values of
the fringe shifts change on time scales comensurate with the duration of
the laser and commensurate with the jitter (or uncertainty) in measuring
the time delay between initiation of the spark column and interferogram.
Since inverted profiles from two different interferograms taken on
different spark columns (though with the same initial conditions) are
subtracted, it is extremely important that the delay time of the two
interferograms be the same. If this condition is not met, deconvolution of
the fringe shift data for comparison to computed results is difficult.

An equivalent comparison between this model and experimental data is
to construct a fringe pattern from the computed densities and compare the
result to the experimentally obtained interferogram. This process requires
one to compute the integral

$$P(x,t) = \frac{2}{\lambda \Delta t} \int_{t-\frac{\Delta t}{2}}^{t+\frac{\Delta t}{2}} \int_0^{R\left[1 - \left[\frac{x}{R}\right]^2\right]^{1/2}} G\left[\left[x^2 + y^2\right]^{1/2}, t'\right] dy \, dt' \qquad [V-2]$$

where now $P(x,t)$ is the simulated transverse fringe shift at time t, Δt is the time duration of the probing laser, λ is the wavelength of interest and $G(r,t)$ is the change in index of refraction from unity as computed with results from the model. $G(r,t)$ has contribution from heavy particles and from electrons. For heavy particles,

$$G_H(r,t) = \gamma \frac{\Delta \rho(r,t)}{\rho_o} \qquad [V-3]$$

where ρ is the mass density, ρ_o is its initial value, and $\Delta \rho$ is the change in mass density from its initial value. The constant γ depends weakly on the gas mix and for our purposes, $\gamma \approx 2 \times 10^{-4}$.[V.2] For electrons, G_e is given by the plasma dispersion relationship.[V.3]

$$G_e(r,t) = -\frac{1}{2} \beta \lambda^2 n_e(t) \qquad [V-4]$$

where n_e is the electron density and in cgs units $\beta = 8.95 \times 10^{-14}$.

The integral over time in Eq. V-2 is necessary because during the time duration of the laser pulse (5 ns), the shock front of the plasma column can move a distance comparable to the resolution of the measurement. Quantities of interest, such as electron density, can also change appreciably during this time. With a velocity of 5×10^5 cm/s, a shock wave can travel a distance of 25 μm during the laser pulse. The result is the fringes are broadened and the apparent thickness of the shock front increased. The thickness of the fringes associated with the undisturbed fringe pattern is accounted for by displacing the simulated fringe patterns by a distance equal to the undisturbed thickness.

V.B. Simulated Interferograms and Comparison to Experimental Data

Experimental interferograms for two Xe/H_2 gas mixes are in Fig. V-1. In Fig. V-1a, the gas mix is Xe/H_2:0.01/0.99 and in Fig. V-1b the gas mix is Xe/H_2:0.03/0.97. The charging voltage is 40 kV and gap spacing is 1.1 cm. The undisturbed fringe pattern is at the extreme right or left of the interferograms. Positive displacements are due to positive $\Delta \rho / \rho_o$, while

negative displacements are due to negative $\Delta\rho/\rho_0$ and electrons. Recall that these interferograms are of line of sight data. The fringe shifts must undergo an Abell inversion to obtain data as a function of radius. The different appearance of the fringes for a relatively small change in gas mixture is dramatic. In the LOS data of Fig. V-1a (Xe/H$_2$:0.01/0.99) there appears to be a rather wide but fairly distinct shell of high heavy particle density. The LOS fringe pattern in the center of the arc appears somewhat circular and is characteristic of a column with a fairly uniform electron density profile. In the LOS data of Fig. V-1b (Xe/H$_2$:0.03/0.97), high density region appears less distinct. The fringe pattern in the center of the arc is flatter than that of the low xenon mixture and has approximately twice the total shift. The transition to the center plateau occurs steeply in a region close to the high high heavy particle shell. This fringe pattern is characteristic of "heavy" gas mixtures, whereas "light" gas mixtures tend to have the more circular fringe pattern.

Simulated interferograms using results from the SPRAD code for the conditions of Fig. V-1 are plotted in Fig. V-2. The qualitative agreement is excellent. The striking difference in the appearance of the fringe pattern is best explained by referring to Fig. V-3, where electron density is plotted as a function of radius for the two cases. For the low xenon case, the electron density, confined within the high mass density shell, is fairly uniform as a function of radius. The electron density penetrates into the shock wave with only a moderate slope. In contrast, the Xe/H$_2$:0.03/0.97 case has a high electron density shell interior to the shock wave. The LOS fringe pattern therefore mimicks that of a thin shell; a flat center with steep sides. The shock wave of the Xe/H$_2$:0.01/0.99 case is somewhat thinner but almost a factor of two higher than that of the the Xe/H$_2$:0.03/0.97 case. The mass density in the interior is rather uniform as opposed to the distribution for the high xenon case which is both higher and has structure.

The differences in shape of the electron density profile, and hence fringe pattern, between the 1% and 3% xenon-hydrogen mixtures results in part from the difference in average molecular weight (3.29 AMU vs 5.87 AMU), and therefore sound speed. The 1% xenon mixture is sufficiently light that the gas responds quickly to pressure gradient. As a result, the convective velocity is positive (radially outward) and the pressure gradient is negative (pressure decreasing radially outward). The molecular weight of the 3% xenon mixture, though, is sufficiently large, and the response time of the gas sufficiently long, that similar conditions cannot be maintained. (See Fig. V-4.) As a result of the lower convective velocity, the high density region interior to the shock is heated thereby

creating a local maximum in pressure. This reverses the pressure gradient, slows the convective velocity interior to the local maximum and may infact reverse the particle flux to be radially inward. A local region of low particle density results. This region has a correspondingly higher E/N and therefore higher rate of ionization. The result is a shell of high electron density interior to the shock.

For certain "heavy" gas mixtures, especially with high fractions of xenon and late in time during the discharge pulse, the fringe pattern exterior to the shock is not flat, An example of which is shown in Fig. V-5. Before reaching the shock, the fringes tilt upward in the direction indicating $\Delta\rho/\rho_o > 1$. For light gas mixtures the transition at the outer edge of the shock is abrupt; that is the fringes remain flat until the shock is reached. A simulated interferogram for similar discharge conditions is in Fig. V-6. Results from the model indicate that the tilted fringes are in fact a result of having $\Delta\rho/\rho_o > 1$ exterior to the shock. For the lighter gas mixtures, the rate of energy deposition as well as the temperature excursion across the shock are both larger thereby resulting in a steeper, thinner shock. For the heavier gas mixtures, the slower rate of energy deposition, as well as a smaller total fraction of deposited energy being available for the thermodynamic expansion, results in an apparently weakening and widening of the shock late in the discharge pulse.
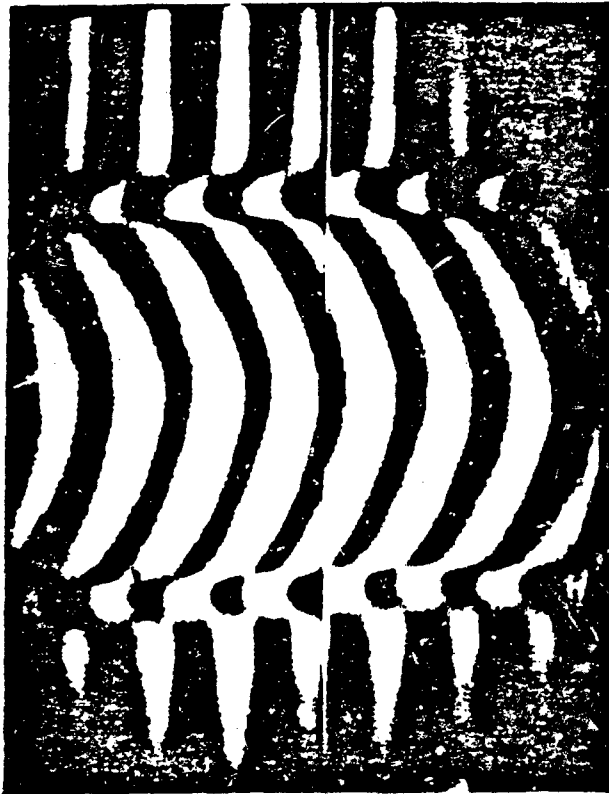
Δt = 50 nsec, w = 0.91 mm
3% Xe/97% H_2
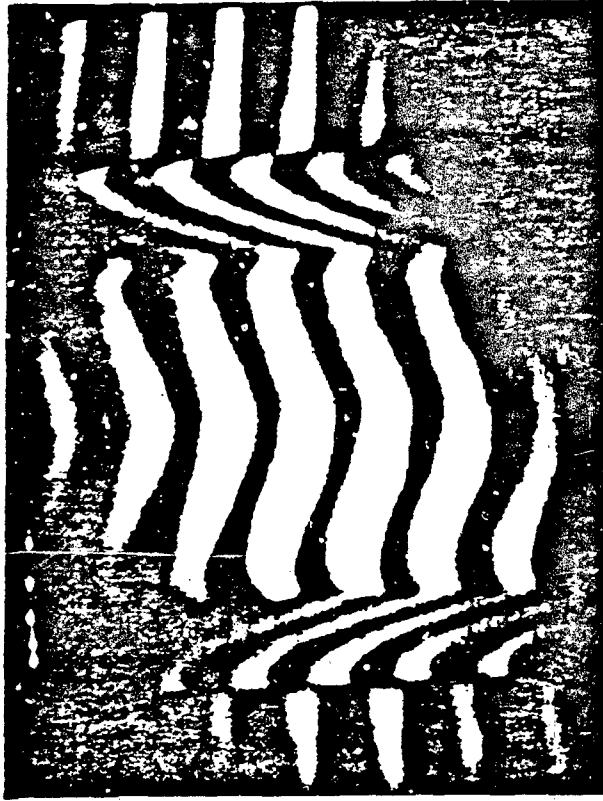
Δt = 38 nsec, w = 0.77 mm
1% Xe/99% H_2

PRESSURE: 1.5 atm abs
V_{peak} ~ 40 kV
DYE WAVELENGTH: 3929 Å

Figure V-1. Experimental Interferograms

V-5
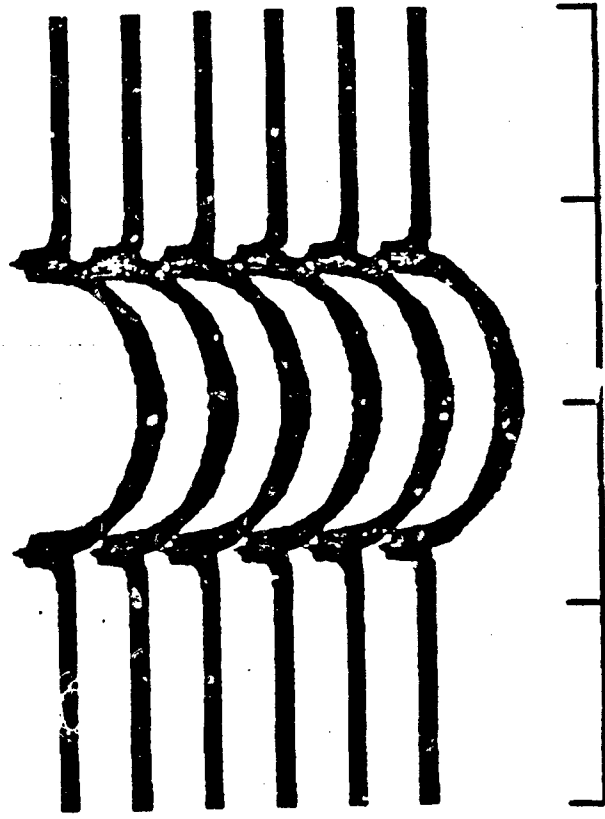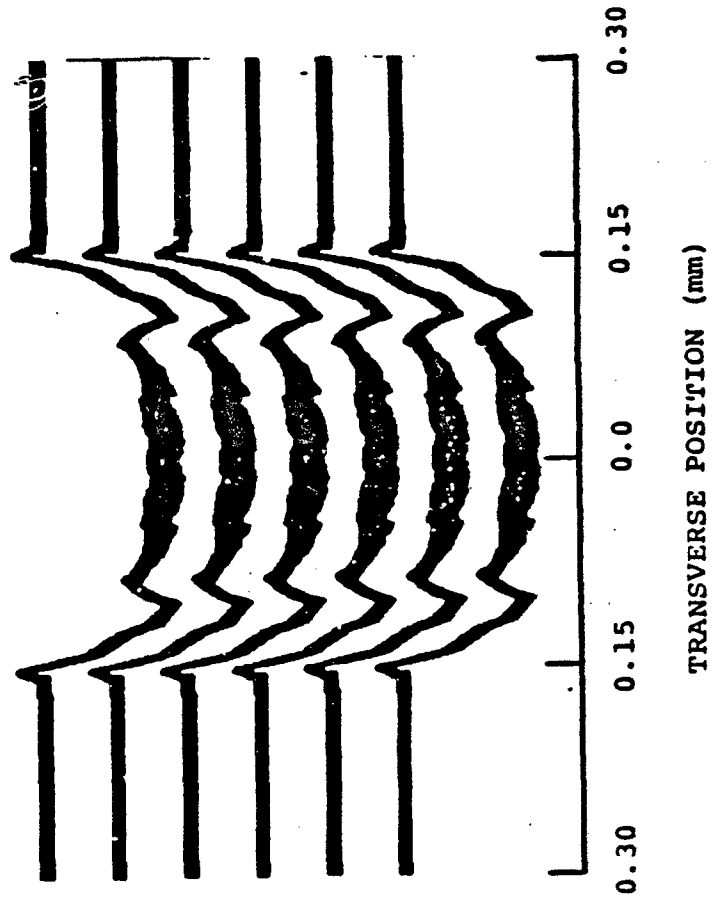
Figure V-2. Simulated Interferograms for the Conditions of Fig. V-1 Produced With the Results of the Model.
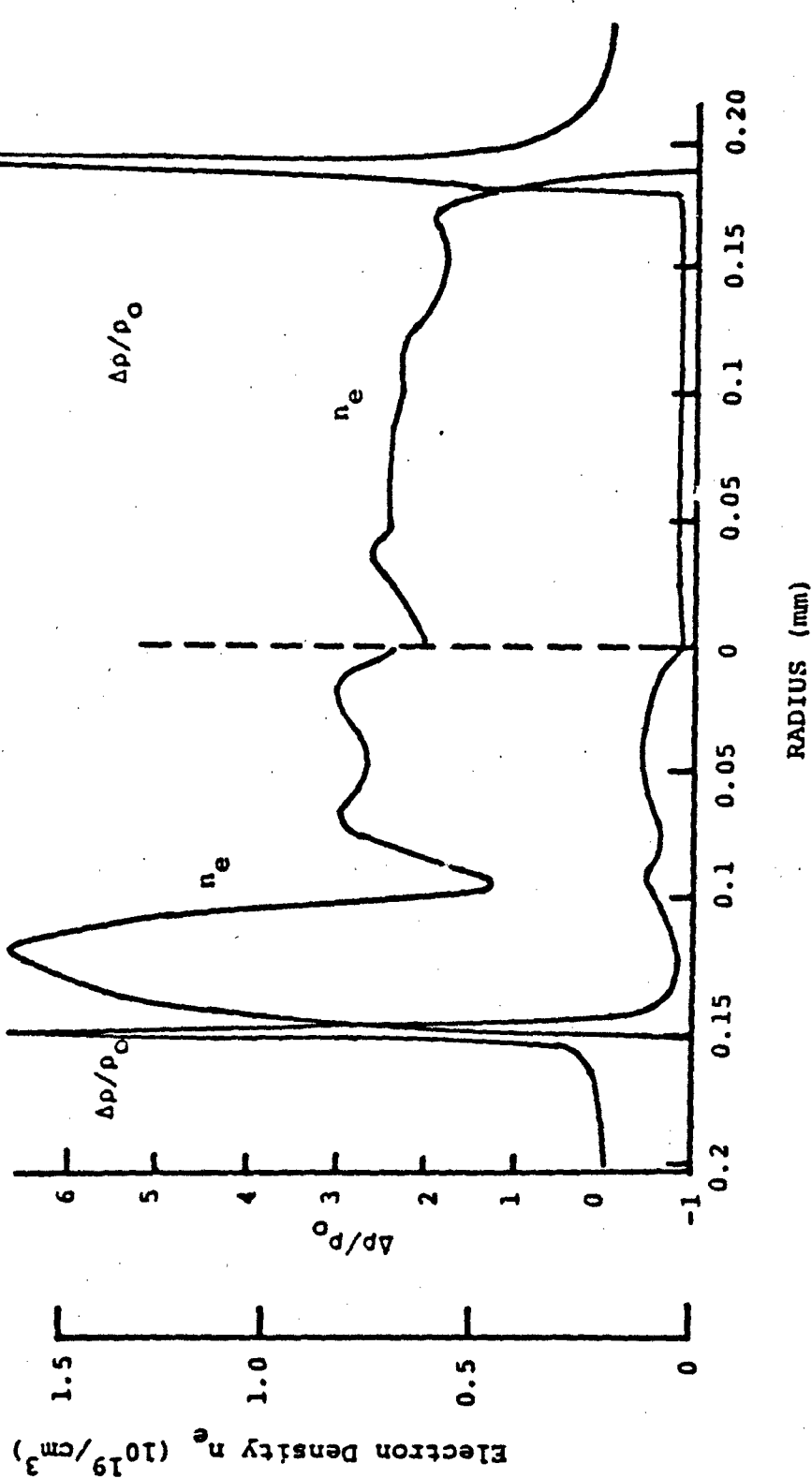
Figure V-3 Mass Density and Electron Density for Spark Columns
in Heavy (Xe/H$_2$:0.03/0.97) and Light (Xe/H$_2$:0.01/0.99)
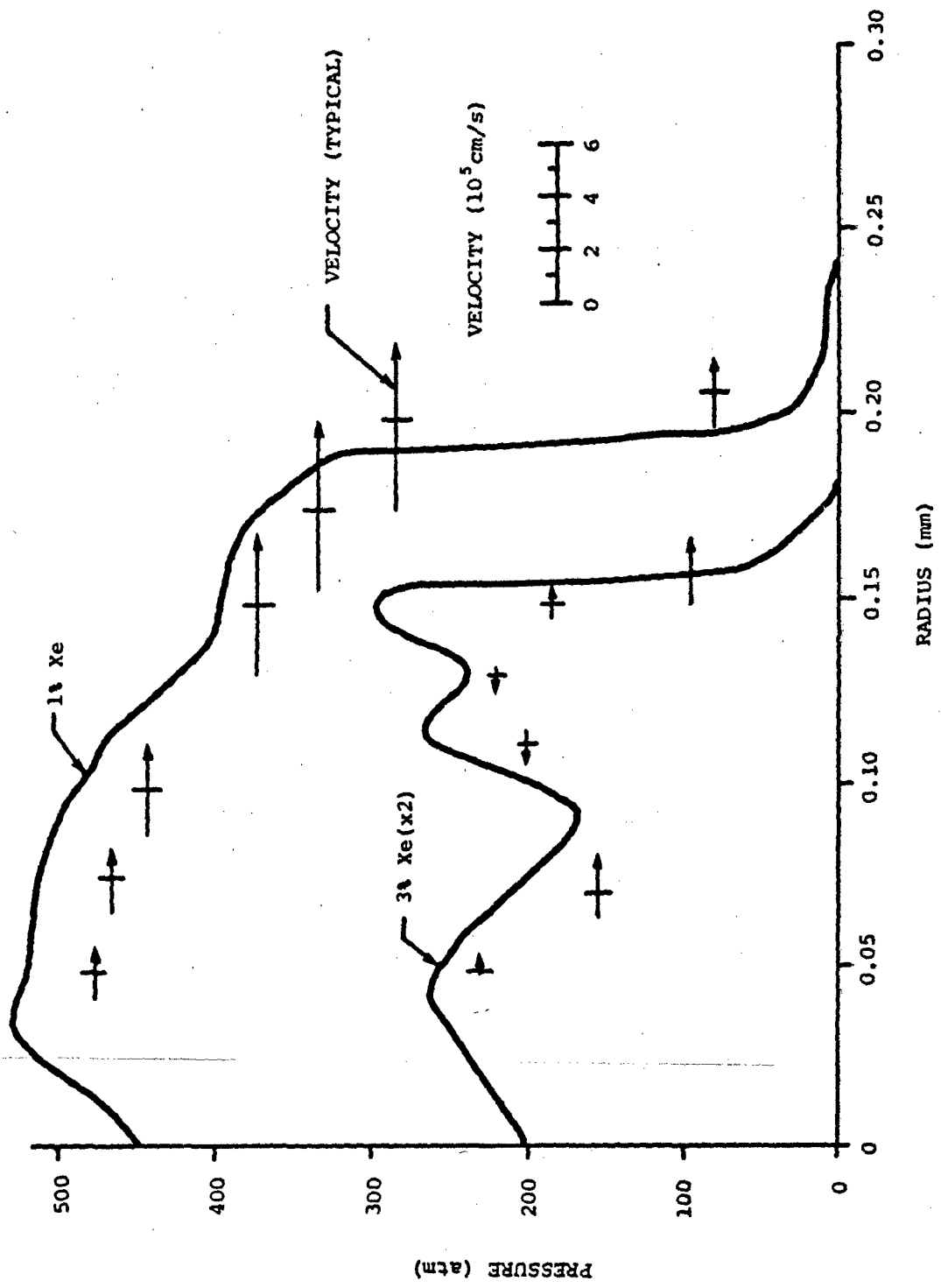
Figure V-4. Convective Velocity for the Conditions of Figure V-3.

84 08737

84 08531
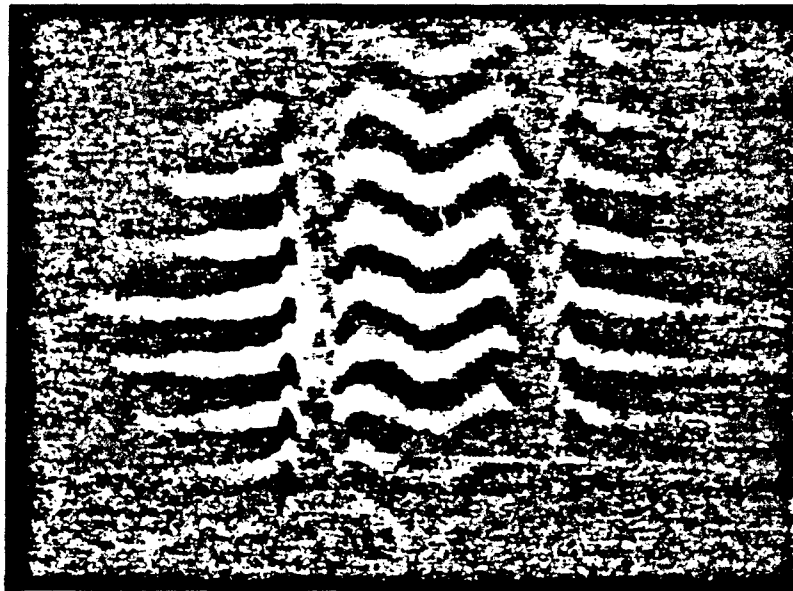
Figure V-5. Experimental Interferogram Showing
Anomalous Fringe Shift

POSITION (mm)

0.30 0.20 0.10 0 0.10 0.20 0.30
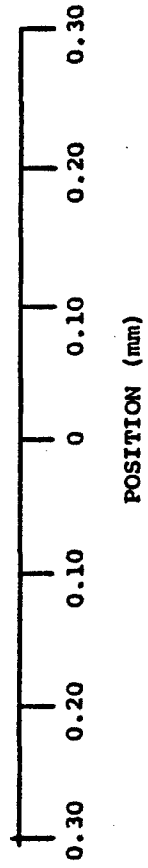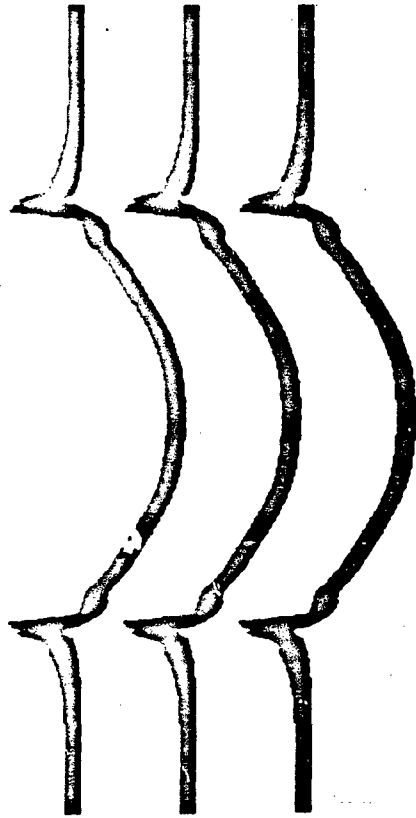
Figure V-6 Simulated Interferogram Showing Anomalous Fringe Shift.

References for Section V

V.1) W. Lochte-Holtgsreven, "Evaluation of Plasma Parameters" in _Plasma Diagnositics_, W. Lochte-Holtgsreven, ed. (Amsterdam: North Holland) 1968.

V.2) R.C. Weast, ed., _Handbook of Chemistry and Physics, 49th Edition_, (Cleveland" Chemical Rubber Co.) 1968, p. E-224.

V.3) F.P. Chen, _Introduction of Plasma Physics_, (New York: Plenum) 1974.

THERMODYNAMICS OF HIGH TEMPERATURE Ar/H$_2$ GAS MIXTURES AND A SIMPLE MODEL FOR LASER TRIGGERED SPARK GAPS

VI.A. Introduction

From the results of our detailed modeling, and the results of our companion experimental program[VI.1], we have learned that arc growth in a laser triggered spark gap can, to first order, be described as a convective expansion of the hot ionized core augmented by thermal- and photo-ionization at its periphery. With have further learned that the interior of the arc is very nearly in local thermal equilibrium. With these facts, a very simple model of a laser triggered spark gap can be constructed. This model is based on an energy balance between joule heating, accumulated internal energy and energy lost by radiation during the duration of the spark. To construct this model, the thermodynamics of Ar/H$_2$ gas mixtures must be known. Although conceptually only a solution of Saha's equation, in practice obtaining the thermodynamic state of an arbitrary gas mixture is difficult. A computationally simple method for obtaining this solution is discussed.

Within the central core of the spark column of a laser triggered spark gap, as well as throughout the hot region of conventional arcs, the thermodynamic state of the plasma is well approximated by assuming local thermodynamic equilibrium (LTE). In 'TE. '.e electron temperature and the heavy particle temperature are equ.. densities of various excited or thermodynamic states of a particular species in the gas are given by their Saha equilibrium values. For charged species,[VI.2]

$$\frac{n_e M^{Z+}}{M^{(Z-1)+}} = \alpha_e \left[\frac{F_{M^{Z+}}(T)}{F_{M^{(Z-1)+}}(T)} \right] \exp\left[\frac{-\left[E_I - \epsilon_L\left[n_e, Z \right] \right]}{kT} \right] \qquad [VI-1]$$

$$\alpha_e = \frac{2\left[\pi k m_e \right]^{3/2}}{h^3} \qquad [VI-2]$$

where n_e is the electron density, m_e is the electron mass, M^{Z+} is the density of species M in charge state Z, and $F_M(T)$ is the partition function for species M. The ionization potential of the higher state relative to the lower state is E_I and the lowering value for the ionization potential (see

below) is $\epsilon_L(n_e, Z)$. For diatomic heavy particle species that may dissociate, the Saha expression for partitioning of densities is,

$$\frac{M^2}{M_2} = \alpha_H \left[\frac{(F_M)^2}{F_{M_2}(T)} \right] \exp\left[\frac{-E_d}{kT} \right] \qquad \text{[VI-3]}$$

$$\alpha_H = \frac{2 \left[\pi k m_H \right]^{3/2}}{h^3} \qquad \text{[VI-4]}$$

where m_H is the mass of the monoatomic species, the density of the diatomic is M_2, that of the monoatomic is M, and the partition functions are F_{M2} and F_M respectively. There may be many excited states permitted within a given ionization state of the heavy particle species. The distribution of these excited states are given by the Boltzmann expression. That is,

$$[N_{ij}] = g_{ij} \exp\left[\frac{-\epsilon_{ij}}{kT} \right] \frac{\sum_j [N_{ij}]}{\sum_{ij} g_{ij} \exp\left[\frac{-\epsilon_{ij}}{kT} \right]} \qquad \text{[VI-5]}$$

where N_{ij} is the density of heavy particles of species i in excited state j, g_{ij} is the statistical weight of N_{ij} and ϵ_{ij} is the excitation potential of the N_{ij} relative to the ground state of N_i. In principle, the sums in Eq. VI-5 diverge because there is an infinite number of excited states as the dissociation or ionization continuum are approached. This problem is circumvented using two methods. For species in which the next higher species (in energy) corresponds to an ion, the ionization potential is lowered from its nominal value. (See below.) This lowering of the ionization potential effectively sets an upper limit to the quantum number for excited states. For diatomic species in which the summation is over vibrational – rotational states, the summation is terminated at a level commensurate with the dissociation energy of the molecule. (See Sec. VI.C.)

In a plasma with a high electron density, the effective ionization potential of atoms is lower than that in the non-ionized gas. This lowering of the ionization potential results from an effective broadening, and hence coalescing, of energy levels near the ionization continuum. Due to the difficulty in measuring this value, only theoretical expressions are available. In this work, the lowering value for the ionization potential, in eV, is given by

$$c_L\left(n_e, Z\right) = 6.96 \times 10^{-7} \, n_e^{1/3} \, Z^{2/3} \qquad\qquad \text{[VI-6]}$$

where the electron density is expressed in cm^{-3}.

VI.B. Method of Solution

We are interested in obtaining all the pertinent heavy particle densities and thermodynamic properties for an arbitrary mix of Ar and H_2 when specifying the total mass density and thermodynamic temperature. Alternately, we would like to obtain the same quantities when specifying the mass density and internal energy of the plasma. The temperature is then a variable for which we solve. For a multi-component plasma, a large system of non-linear equations consisting of the appropriate Saha equations must be solved. Traditionally, large matrix inversions are performed to achieve this end. For our system of equations where we specify the total mass density we can exploit the principle of conservation of mass and charge in order to obtain an iterative solution which converges rapidly. For a gas with a total density of Ar atoms of Ar_T

$$Ar_T = \sum_{\ell=0}^{\ell=\ell_{max}} Ar^{\ell+} \qquad\qquad \text{[VI-7]}$$

where $Z = \ell_{max}$ is the maximum ionization state of Ar of interest. Note that the Saha equation for $Ar^{\ell+}$ can be written as

$$Ar^{\ell+} = \frac{Ar^{(\ell-1)+} \, D_\ell\left(T, n_e\right)}{n_e} \qquad\qquad \text{[VI-8]}$$

where $D_\ell(T, n_e)$ contains the ratio of partition functions and Boltzmann factor. The dependence of D_ℓ on electron density is through the value of c_L and therefore is weak. Therefore, in an iterative fashion, we can write

$$Ar^{\ell+} = Ar^0 \, \frac{\prod\limits_{i=1}^{i=\ell} D_i}{n_e^\ell} \qquad\qquad \text{[VI-9]}$$

The kernal value for Ar^0 is obtained from

$$Ar^0 = \frac{Ar_T}{\left[1 + D_1/n_e + D_1D_2/n_e^2 + \cdots + \dfrac{D_1D_2 \cdots D_\ell}{n_e^\ell} \right]} \qquad \text{[VI-10]}$$

We can write analogous expressions for the hydrogen species. For a total density of hydrogen atoms of H_T,

$$H_T = H + H^+ 2 \cdot H_2 + 2 \cdot H_2^+ \qquad \text{[VI-11]}$$

$$H^+ = \frac{F_1[T,n_E]H}{n_e}, \qquad H_2^+ = \frac{F_2[T,n_e]H_2}{n_e}, \qquad H^2 = F_3(T)H_2 \qquad \text{[VI-12]}$$

Note that Eq's. 12 have as a kernal H_2. Solving for the value of H_2 as a function of H_T, we obtain

$$H_2 = \left[\frac{J}{2K} \left[\left(1 + \frac{4H_TK}{J^2} \right)^{1/2} - 1 \right] \right]^2 = F_5(n_e) \qquad \text{[VI-13]}$$

where $J = F_3^{1/2}(1 + F_1/n_e)/2$ and $K = (1 + F_2/n_e)$. The problem is then solved by obtaining the kernals from Eq's. 10 and 13, which reduces to solving for the electron density. This last value is obtained by noting that for our system,

$$n_e = H^+ + H_2^+ + \sum_{\ell=1}^{\ell=\ell_{max}} \ell Ar^{\ell+} \qquad \text{[VI-14]}$$

The iterative solution consists of specifying Ar_T, H_T, and an initial guess for n_e. New values for the ionic species are obtained by first obtaining values for the kernals from Eq's. 10 and 13, and a new value for n_e is obtained from Eq. VI-14. This process repeats until the solution converges to the desired accuracy. Only tens of iterations are usually required for this method to converge to an accuracy of 10^{-6}.

VI.C. Partition Functions

The partition function for a diatomic molecular species is given by the sum(VI.3)

$$P = \frac{1}{2} \sum_{0}^{v_{max}} \sum_{}^{J_{max}} (2J + 1)\exp\left[\frac{-(E(v,J)-E(0,0))}{kT}\right] \qquad \text{[VI-15]}$$

$$E(v,J) = \left[v + \frac{1}{2}\right]\omega_e + \left[v + \frac{1}{2}\right]^2 \omega_e x_e \left[v + \frac{1}{2}\right]^3 \omega_e y_e + B_e J(J + 1) \qquad \text{[VI-16]}$$

$$- D_e J^2 (J + 1)^2 - \alpha_e J(J + 1)\left[v + \frac{1}{2}\right] - \beta_e J^2 (J + 1)^2 \left[v + \frac{1}{2}\right]$$

where ω_e, x_e, y_e, B_e, D_e, α_e, and β_e are the usual spectroscopic constants and are listed in Table VI-1 for H_2 and H_2^+. The values of J_{max} and v_{max} for H_2 were obtained from Ref. VI.4. For H_2^+, the value for J_{max} for a given v was obtained from solving

$$E\left[v,J_{max}\right] - E(0,0) = D_o \qquad \text{[VI-17]}$$

where D_o is the H_2^+ dissociation energy (2.65 eV). The value of v_{max} was obtained by setting $J_{max} = 0$ in Eq. VI-17 and solving for v.

For monoatomic species, the partition function is

$$P = \sum_{\ell=0}^{\ell = \ell_{max}} g_\ell \exp\left[\frac{-\left[E_\ell - \epsilon_L\left[n_e, Z\right]\right]}{kT}\right] \qquad \text{[VI-18]}$$

For both Ar and H, we obtained values for g_ℓ and E_ℓ from Ref. VI.5. For Ar, we calcuated values for ionization states up to and including Ar^{5+}. To reduce the number of levels to a managable size, excited states of Ar were grou_ _d into psuedo states which contained all levels within an energy width of approximately 1500 cm^{-1}. The statistical weight of a given pseudo state was then the sum of the statistical weights of all real levels contained within the energy bin.

VI.D. Thermodynamic Quantitities and Transport Coefficients

After solving for the number densities of the different species in the plasma, various thermodynamic quantities and transport coefficients can be obtained. Three quantities of interest are the internal energy, electrical conductivity and radiation energy loss. Assume we have quasi-steady state conditions and that out time scale of interest is long compared to the thermal equilibration time of a given column of gas, but short compared to the thermal conduction of energy exterior to the column. For these conditions, the internal energy of the plasma is maintained by a

balance between power input to the column from joule heating (proportional to the conductivity of the plasma) and power lost from the column by emission of radiation. In principle, the internal energy of the plasma can be arbitrarily large or small since the energy balance (in the steady state) depends only on the equilibration of the energy input and radiation losses. The time required to reach the steady state value of the internal energy depends on the initial defect in the rate of joule heating to that of radiation loss.

The internal energy of the plasma is simply

$$E_{int} = \sum_{i,j} \left[N_{ij}\left(E_{ij} + \frac{2}{(\gamma_i - 1)} kT\right)\right] + \frac{3}{2}n_e kT \qquad [VI-19]$$

where N_{ij} is the density of species i excited to level j, E_{ij} is its excitation energy relative to Ar(Z=0, n=0) or H_2(v=0), and γ_i is the ratio of specific heats. The terms in Eq. VI-19 are for electronic, vibrational, and ionization energy stored within each species, translational energy of the heavy particles and translational energy of the electrons.

To obtain the rate of radiation loss, one must know the emissivity of the plasma. For a cylindrical plasma of diameter d and length L, where d/L ≪ 1, the emissivity at frequency ν, $\epsilon(\nu,d)$ can be approximated by[VI.6]

$$\epsilon(\nu,d) \approx 1 - \exp\left[\frac{\alpha(\nu)d}{\left(1 + 0.7(\alpha(\nu)d)^{1/2} + 0.08\alpha(\nu)d\right)}\right] \qquad [VI-20]$$

where the photon absorption coefficient is $\alpha(\nu)$. With $\epsilon(\nu,d)$, the volumetric rate of energy loss from the cylinder due to radiation, E_{rad}, is obtained by integrating the Planck function over wavelength;

$$E_{rad}(T,d) = \frac{4}{d} \int_0^\infty \epsilon(\nu)\frac{2\pi h\nu^5}{c^3\left[\exp\left(\frac{h\nu}{kT}\right) - 1\right]} \, d\nu \qquad [VI-21]$$

Absorption coefficients used for this calculation are identical to those described in section II. B.

The electrical conductivity of a plasma,

$$\sigma_e = \frac{e^2 n_e}{m_e\left[\nu_{CN} + \frac{\nu_{cI}}{1.975}\right]} \qquad [VI-22]$$

VI-6

is a proportional to the electron density and inversely proportional to the electron collision frequency. The electron collision frequency is the sum of two terms, collisions with neutrals, ν_{cN}, and collisions with ions, ν_{cI}. As the ion density, and hence ion collision frequency, becomes comparable to that of the neutrals, the electrical conductivity asymptotes to a maximum value, called Spitzer's conductivity. Once this limit is reached, from ion density considerations, the electrical conductivity can only increase by increasing the temperature of the plasma. For sufficiently dense plasmas, called non-Debye plasmas, the assumptions with which the ion collision frequency is derived are no longer valid. The limit of validity is when there is less than one electron within a Debye sphere, that is the mean separation between electrons is less than a Debye length. When this limit is reached, the electrical conductivity decreases from the Spitzer value. In the Spitzer formulation, the electron collision frequency in a plasma with temperature T, summed over ions with density N_i and charge Z_i is $^{(VI.7)}$

$$\nu_{cI} = \sum_i N_i \frac{4(2\pi)^{1/2}}{3} \left[\frac{m_e}{kT}\right]^{3/2} \left[\frac{e^2}{4\pi\epsilon_o m_e}\right]^2 \ell n\Lambda \qquad [VI-23]$$

$$\Lambda = \frac{12\pi\epsilon_o^{3/2}(kT)^{3/2}}{Ze^{5/2} n_e^{1/2}} \qquad [VI-24]$$

The last factor in Eq. VI-23, $\ell n\Lambda$, is obtained assuming that $\Lambda \gg 1$, which is the condition for a Debye plasma. The first order correction for non-Debye plasma, that is when the inequality involving Λ does not hold, is to replace the above factor with its exact expression;

$$\ell n\Lambda \rightarrow \frac{1}{2}\left[\ell n\left(1 + \Lambda^2\right) - \frac{\Lambda^2}{1 + \Lambda^2}\right] \qquad [VI-25]$$

In the limit that $\Lambda \gg 1$, Eq. VI-25 reduces to $\ell n\Lambda$.

VI.E. Simple Scaling Model for Spark Column

Given the values for electrical conductivity and rate of radiation loss, a simple scaling model for spark columns can be constructed. For a given mass density and gas mix, we can calculate $\sigma_e(T)$ and $E_R(T)$. For a total current I conducted through the spark column, having current density j, and diameter d ($I = j\pi d^2/4$), energy conservation requires that

$$E_{int}(T) = \left[\frac{i^2}{\sigma_e(T)} - E_{rad}(T,d)\right] \Delta t \qquad [VI-26]$$

where Δt is the time duration of the spark. Eq. VI-26 states that the energy difference between joule heating and that which is radiated away must equal the internal energy of the plasma. Recall that these relationships critically depend on the cylindrical nature of the plasma and the validity of the assumption of local thermodynamic equilibrium. For a given total current, $E_{rad}(T,d)$, $E_{int}(T)$ and $\sigma_e(T)$, Eq. VI-25 can be satisfied by a set of values for arc diameter, d, and temperature, T. In order to obtain a unique solution, we must have another relationship between d and T. To obtain this relationship, a model must be constructed describing the expansion of the arc for a given temperature. Satisfying this requirement is the motivation for the detailed kinetics, hydrodynamics and radiation transport model discussed in previous sections. For purposes of obtaining such a relationship to apply in this simple model, we assume that the arc diameter results from a combination of sonic expansion of the initial arc column, augmented by a non-convective component due to radiation transport and thermal shock heating of neutral gas. Using this model, the final arc diameter as a function of temperature of the plasma is

$$d_f = \beta\left[d_i + 2\left[\frac{\gamma(T)kT}{M}\right]^{1/2} \Delta t\right] \qquad [VI-27]$$

where β is the non-convective augmentation of the arc expansion (equal to 1 for a purely sonic expansion), d_i is the initial arc diameter, γ is the ratio of specific heats, and M is the mean molecular weight of the gas mixture. If we assume that as a result of the non-convective expansion of the arc, mass is entrained into the plasma, then the final mass density of the arc (neccessary for the calculation) is

$$\rho_f = \rho_i \frac{\left[d_i^2 + d_f^2 \frac{\left[\beta^2 - 1\right]}{\beta^2}\right]}{d_f^2} \qquad [VI-28]$$

where ρ_i is the initial mass density.

VI.F. Results from the Thermodynamic Model for Mixtures of Ar/H$_2$

Number densities for a plasma in a mixture of 0.5/0.5:Ar/H$_2$, as calculated with the thermodynamic model, are plotted in Fig. VI-1. For

these results, the mass density is constant and corresponds to 1 atm at room temperature ($\rho = 8.6 \times 10^{-4}$ g/cm^3). The values are plotted as the ratio of number density divided by the total number density of all species in the plasma including electrons. (Recall that the total number density increases with increasing temperature as a result of ionization and dissociation.) As the temperature increases, the density of Ar I decreases and the density of Ar II increases. As the temperature increases further, higher ionization states become the dominant Ar species. The density of H_2 monotonically decreases as it is thermally dissociated. The density of atomic hydrogen increases at low temperatures, a result of dissociation of H_2, but decreases at temperatures greater than about 1 eV due to ionization. The density of H_2^+ is never very large.

The electrical conductivity for the 0.5/0.5:Ar/H_2 gas mix is plotted as a function of temperature in Fig. VI-2. The approach to Spitzer conductivity is clearly indicated as the neutral molecular and atomic species are dissociated and ionized, leaving a fully ionized plasma. The Spitzer limit is indicated by a straight line on the log-linear plot.

Photon absorption coefficients as a function of photon energy and temperature are plotted in Fig. VI-3. The atomic levels were not Stark or Dopplar broadened in calculating these values. At low temperatures, there is structure in the wavelength dependence of the absorption coefficient as a result of ionization of excited states of H and Ar I. At the higher tempertures, we have two local maxima in aborption. The maximum in absorption at low photon energies is due to inverse Brehmstrallung. For low temperatures, first excited states of H and Ar I have appreciable densities, thereby accounting for the absorption peak around 4 eV. As these atoms are ionized, and inverse Brehmstrallung becomes more important, this peak is lost to the continuum. The second maximum in absorption, occuring from 12 to 15 eV, is due to photo-ionization of ground state H and Ar I. The gradual shift of the threshold value of this peak to lower values as the temperature increases is due to the lowering of the ionization potential. The reduction in the absolute value of the peak at higher temperatures is due to the ionization, and subsequent depletion of the ground state.

Power radiated from the plasma cylinder, for LTE conditions, as a function of wavelength and temperture is plotted in Fig. VI-4. At sufficiently high temperature, the emission appears thermal in character. The sudden jump in power loss at approximately 12 eV is a result of the large emissivity for photons with that energy and above. An observer far from the plasma column, measuring the photon flux through a depth of

neutral gas, would not see these photons as they would be absorbed in the
intervening gas. These photons are absorbed in the shock front which
confines the expanding plasma column, and are in fact the mechanism
responsible for the non-convective component of the expansion. To the
extent that these photons are initially absorbed in a region of gas which
does not carry current, the UV photons can be considered as being lost from
the system with respect to the energy balance. In reality, the plasma
column is not a perfect cylinder but has a gradient in temperature and
electron density between the plasma core and cold gas exterior to the
core. These UV photons are absorbed in the gradient region where the
current density is small as compared to the core. Therefore, the
assumptions made for this analysis remain valid.

As discussed above, the energy balance relationships between internal
energy, radiation loss, and the heating (Eq. VI-28) do not define a
unique relationship between diameter and temperature of the spark column.
The expansion model (Eq. VI-29) is required to obtain this relationship.
An example of these relationships are in Fig. VI-5, where arc radius as a
function of diameter of the plasma column is plotted for total currents of
1-10 kA. The gas mix is $0.5/0.5:Ar/H_2$. The initial pressure of the cold
gas is 2 atm and the initial diameter of the spark is 100 μm. The non-
convective (ie.: radiative) augmentation to the convective expansion is β
= .5, and the spark duration Δt = 125 ns. For a given temperature,
larger diameter sparks are required to carry larger currents. Analogously,
at a constant diameter, a higher temperature plasma will carry higher
currents because the conductivity increases with increasing temperature.
There is a large motiviation, with respect to minimizing the loss of energy
from the plasma, to maximize the diameter of the column. The rate of
energy loss due to radiation is proportional to the surface area of the
column while the rate of joule heating is proportinal to the volume of the
column. Therefore, having a plasma column with a larger diameter reduces
the relative loss of energy to radiation. This enables a higher
temperature, larger conductivity, and higher current carrying ability for a
given amount of joule heating.

Fig. VI-5 also contains a plot of Eq. VI-29, the model for arc
expansion, which defines the relationship between diameter and
temperature. The intersection of the line of this plot with those lines
defining the allowed values of d and T (based on energy conservation) for a
given value of current establishes the plasma conditions for that
particular current. Arc diameters and temperatures for different mixtures
of Ar/H_2, obtained in this manner, are plotted in Fig. VI-6. The initial
pressure is 2.0 atm. As the mole fraction of H_2 increases, the arc

diameter increases as a result of the reduced average molecular weight having a correspondingly larger sound speed. In the Spitzer limit, the conductivity depends only on plasma temperature. Therefore to carry a given current, an arc of smaller diameter (ie.: large mole fractions of argon) must be at a higher temperature. Analogously, as the mole fraction of hydrogen increases and diameter of the arc increases (due to the larger sound speed), for a given total current the required plasma temperature decreases.

Arc diameters and plasma temperatures with an initial mix of 0.5/0.5:Ar/H$_2$ as a function of current are plotted in Fig. VI-7. Results for initial pressures of 1-3 atm are plotted. Since the speed of sound depends only on the ratio of specific heats and molecular weight, and not on density, the diameter of the arc changes little as a function of pressure for a given current. What change there is due primarily to a change in temperature. For a given current the plasma temperature increases with increasing pressure. When the initial number density decreases, the ion density corresponding to the Spitzer limit represents a larger fractional ionization thereby requiring a temperature. To obtain this fraction, a higher temperature is required.

TABLE VI-1

Spectroscopic Constants of H_2 and H_2^+ (cm^{-1}) [†]

	H_2	H_2^+
ω_e	4395.2	2297.
$\omega_e x_e$	117.99	62.
$\omega_e y_e$	0.29	—
B_e	60.809	29.8
α_e	2.993	1.4
D_0	36,045.	21,324.

$$\beta_e = D_e \left[\frac{8\omega_e x_e}{\omega_e} - \frac{5\alpha_e}{B_e} - \frac{\alpha_e^2 \omega_e}{24B_e^3} \right]$$

$$D_e = D_0 + \frac{1}{2}\omega_e - \frac{1}{4}\omega_e x_e + \frac{1}{8}\omega_e y_e$$

[†] Ref.: G. H. Herzberg, <u>Molecular Spectra and Molecular Structure</u> <u>I. Spectra of Diatomic Molecules, 2nd Edition</u>, Van Nostrand, New York, 1950.
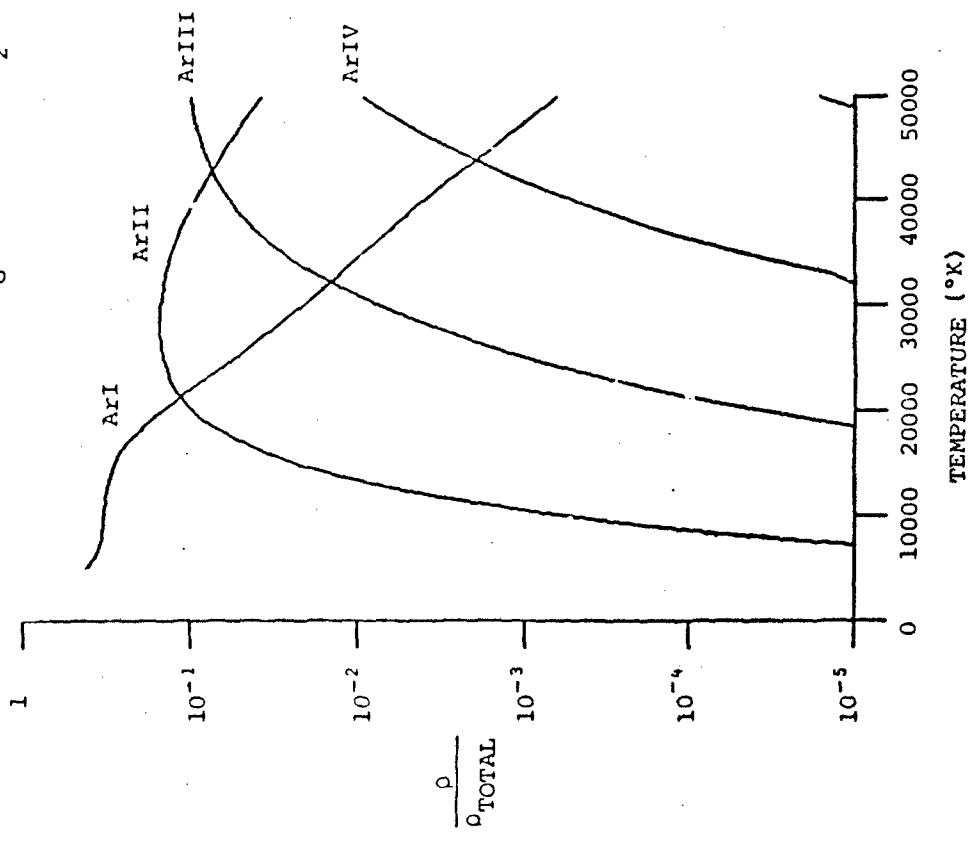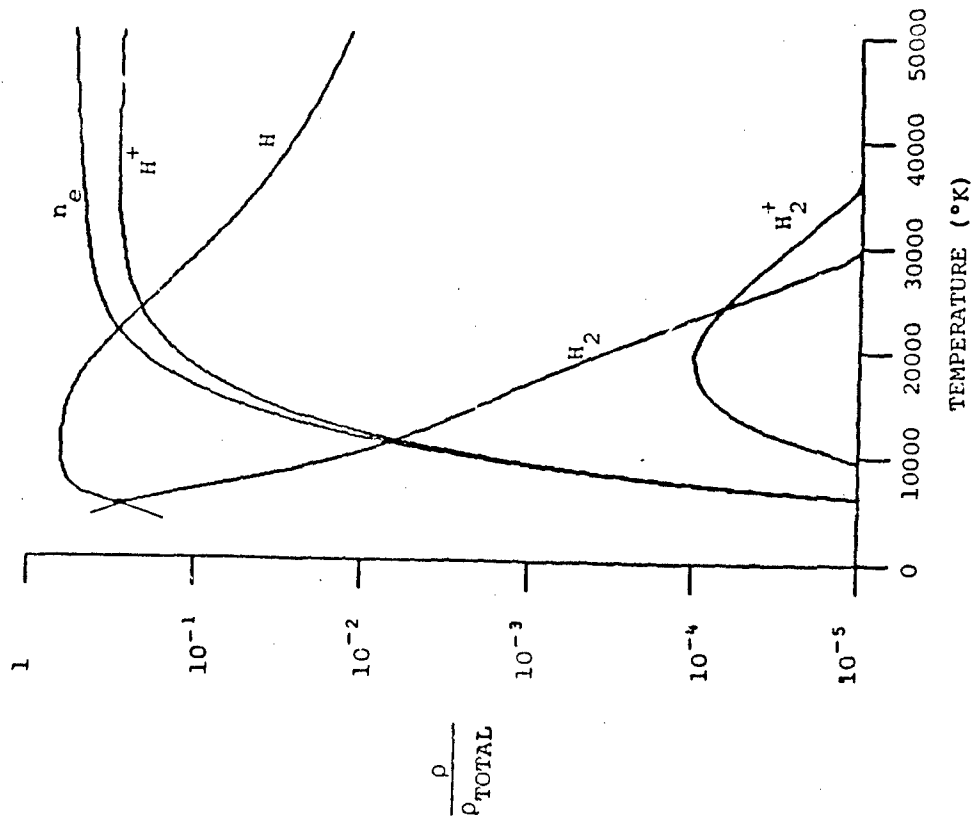
Figure VI-1 Fractional Number Density of Species in an Ar/H_2:0.5/0.5
Gas Mixture as a Function of Temperature
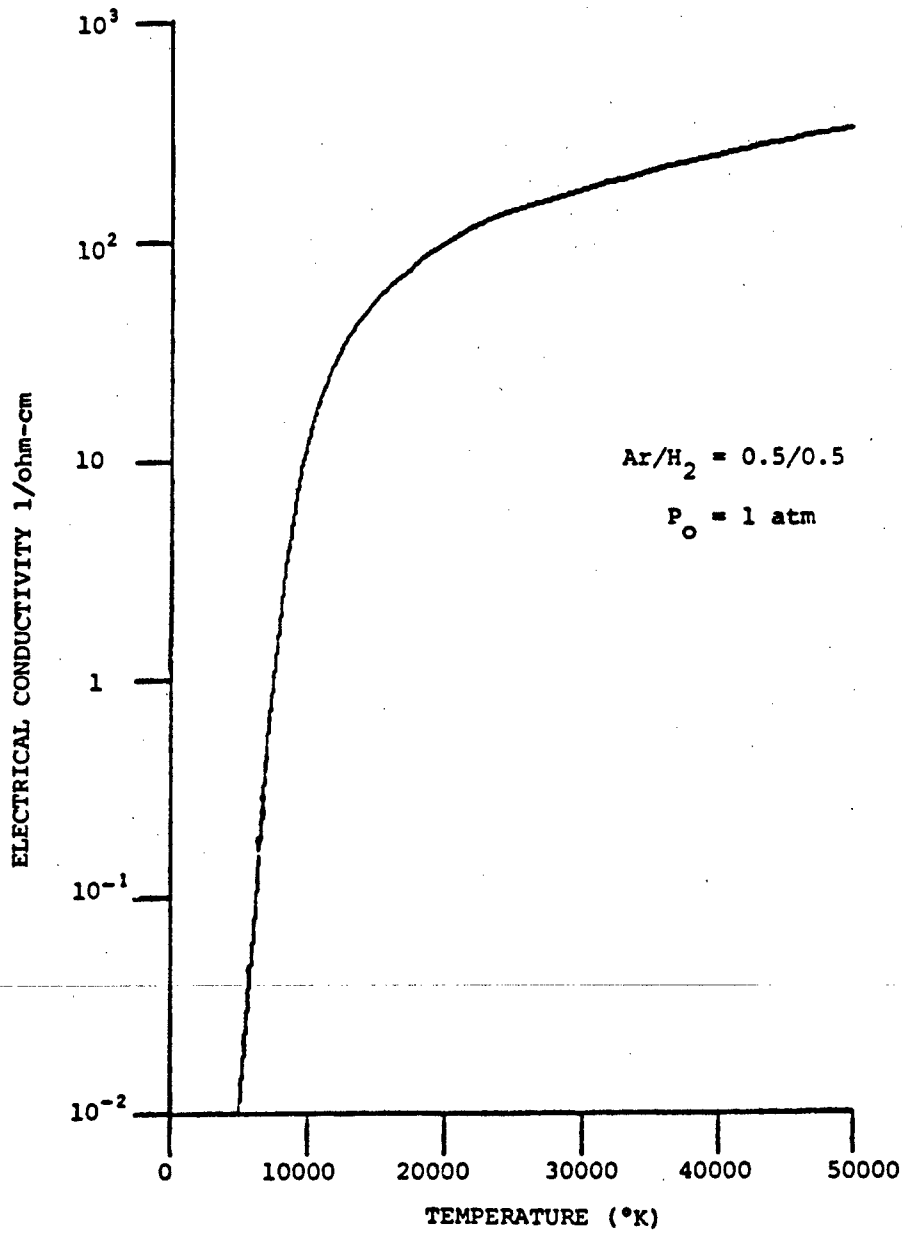
Figure VI-2. Electrical Conductivity for an Ar/H$_2$:0.5/0.5 Gas Mixture as a Function of Temperature.
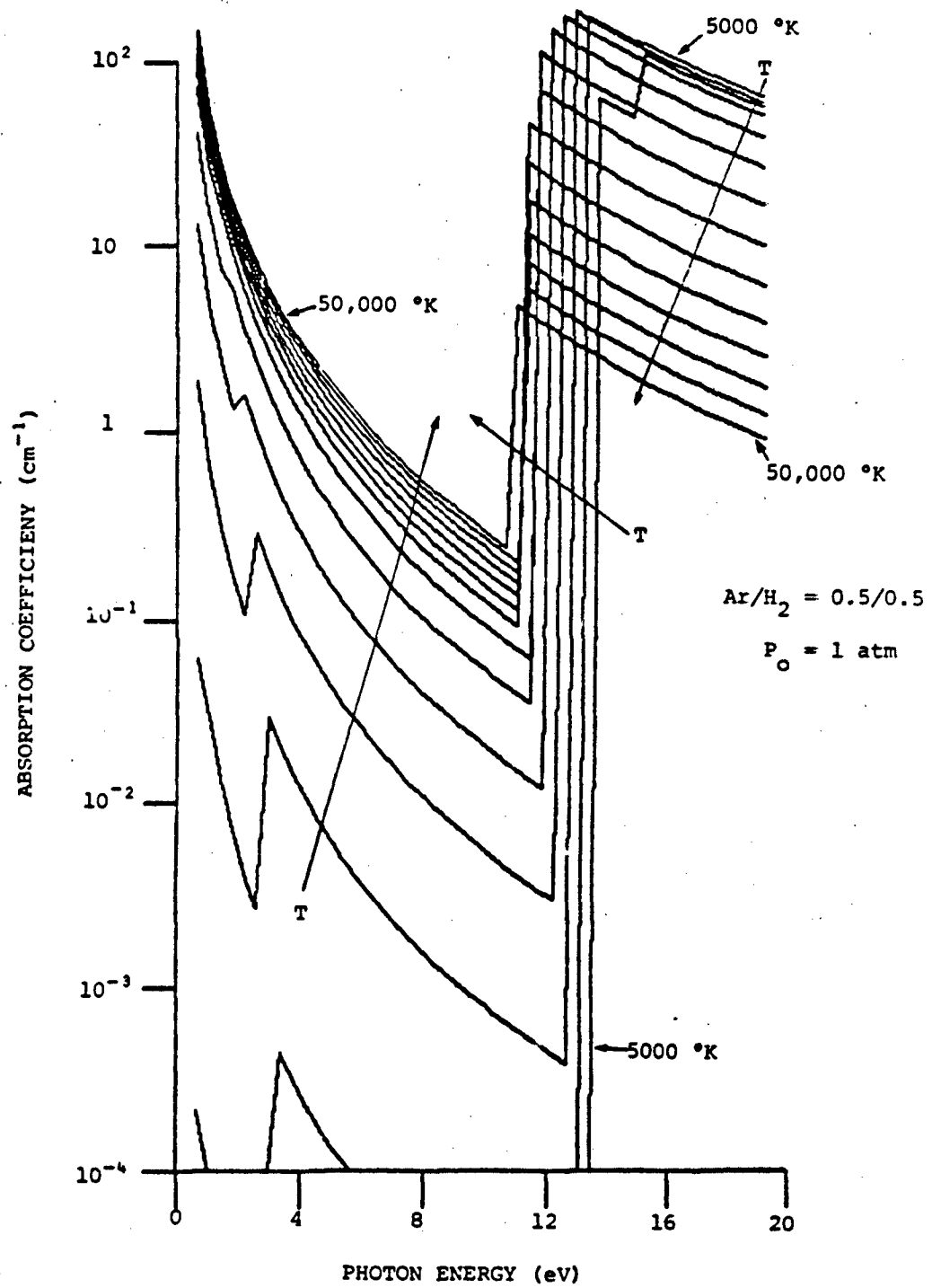
**Figure VI-3** Optical Absorption Coefficient for an Ar/H₂:0.5/0.5 Gas Mixture as a Function of Temperature and Photon Energy.

VI-15
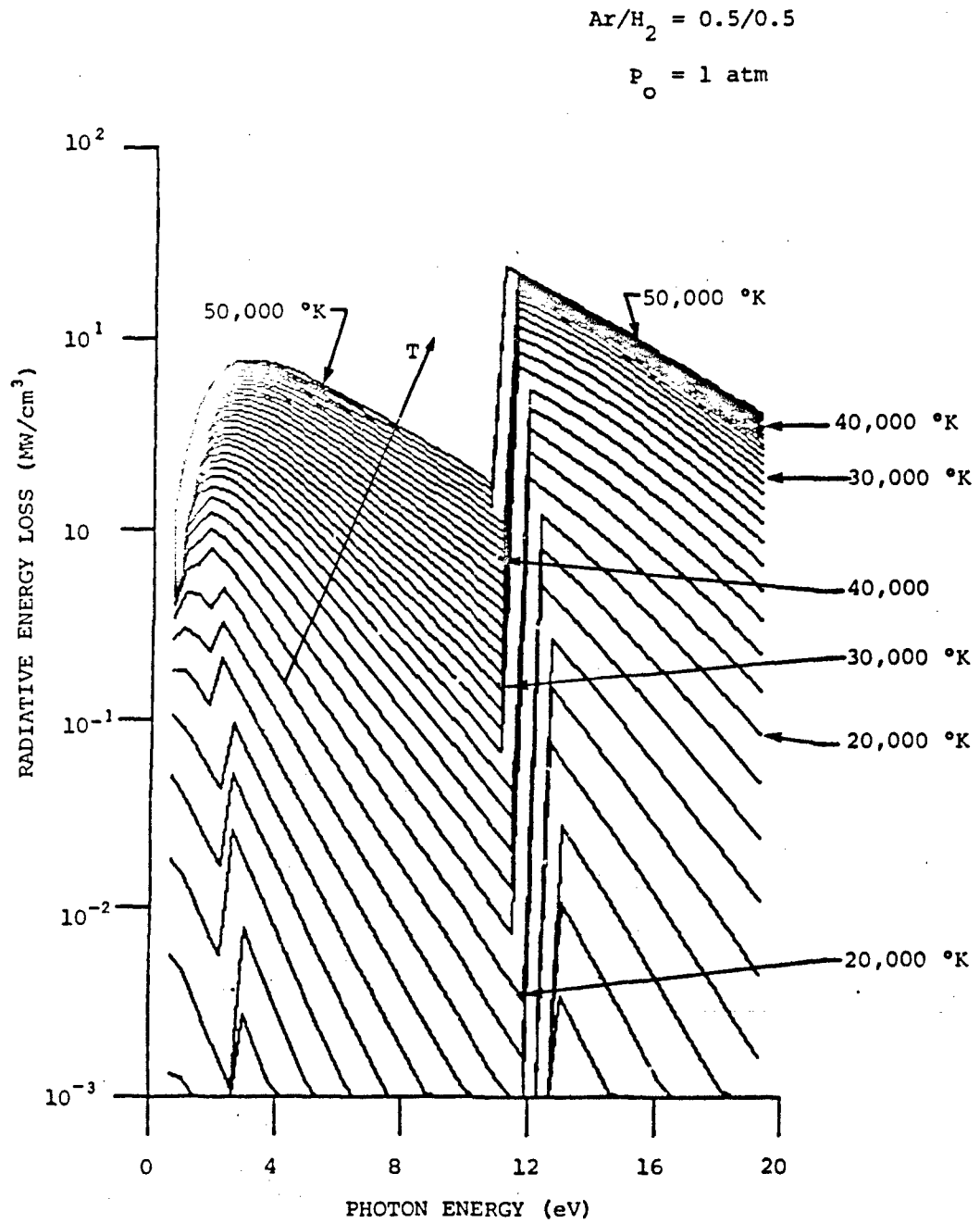
Figure VI-4. Radiative Energy Loss from a Spark Column in an
Ar/H$_2$:0.5/0.5 Gas Mixture as a Function of
Temperature and Photon Energy.

VI-16
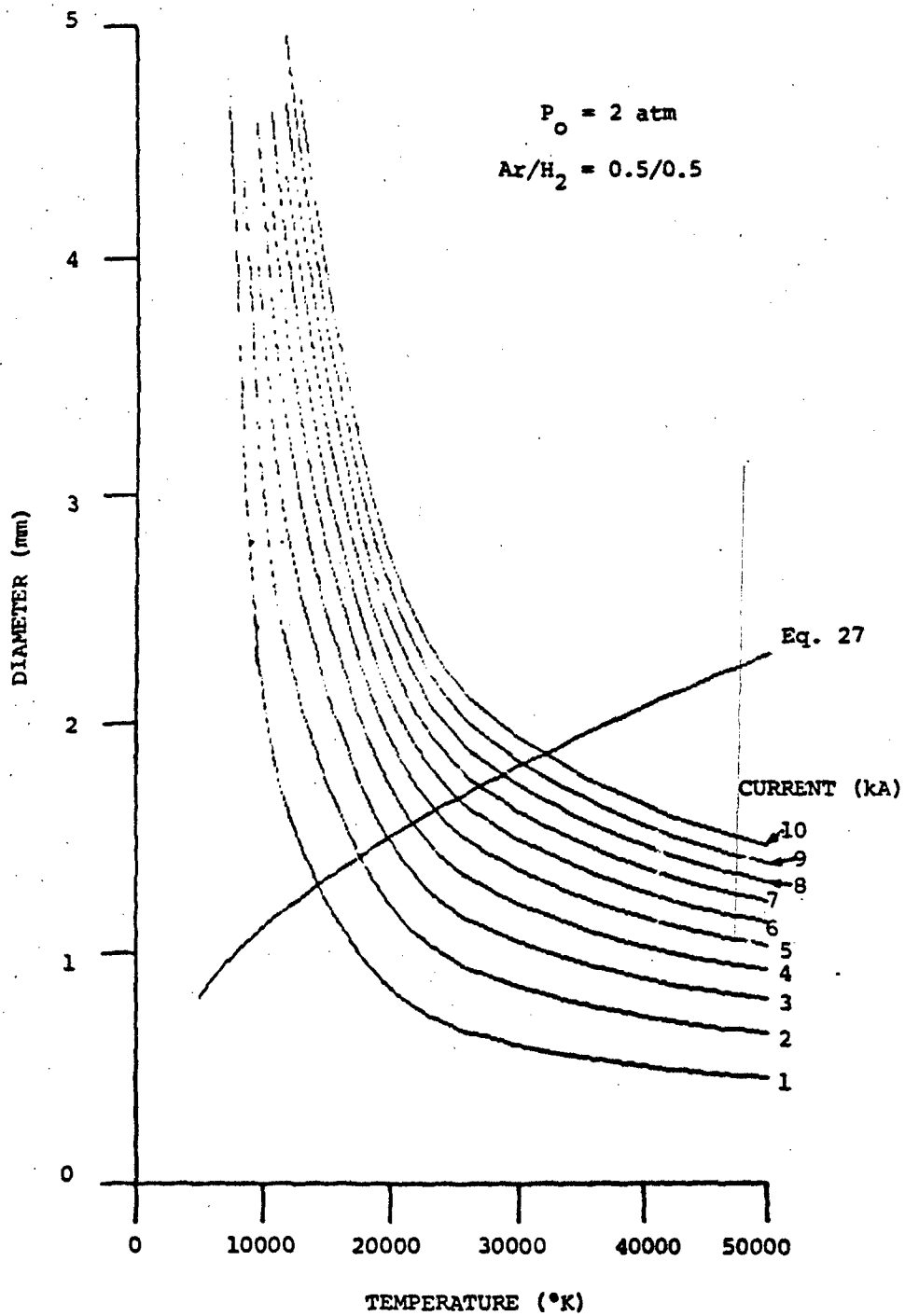
Figure VI-5 Arc Diameter for an Ar/H_2:0.5/0.5 Gas Mixture as a Function of Temperature and Total Current.
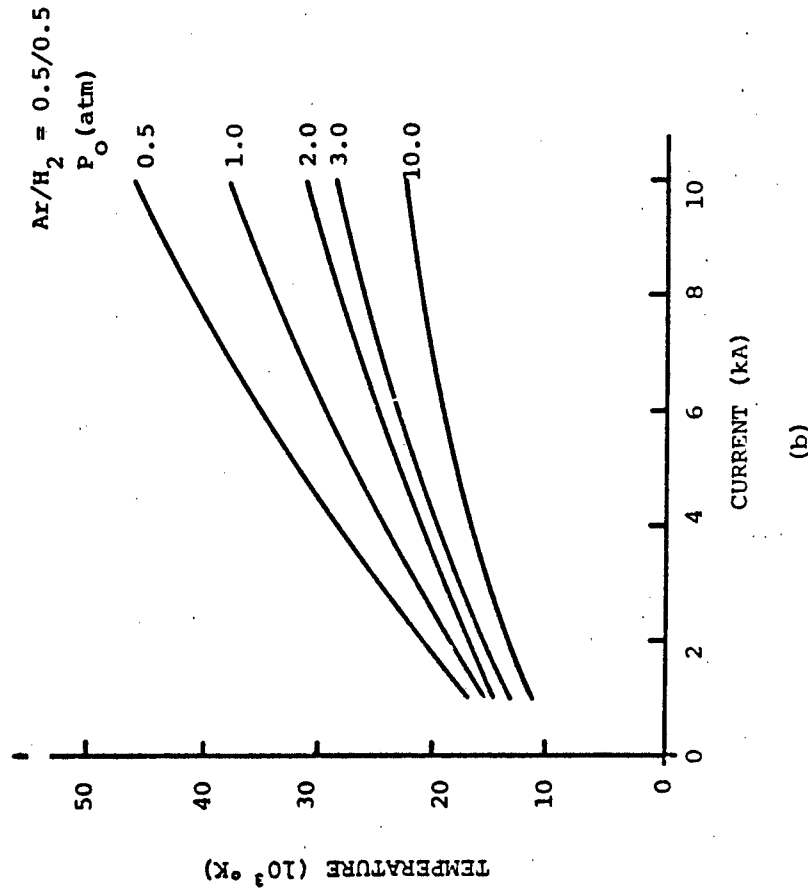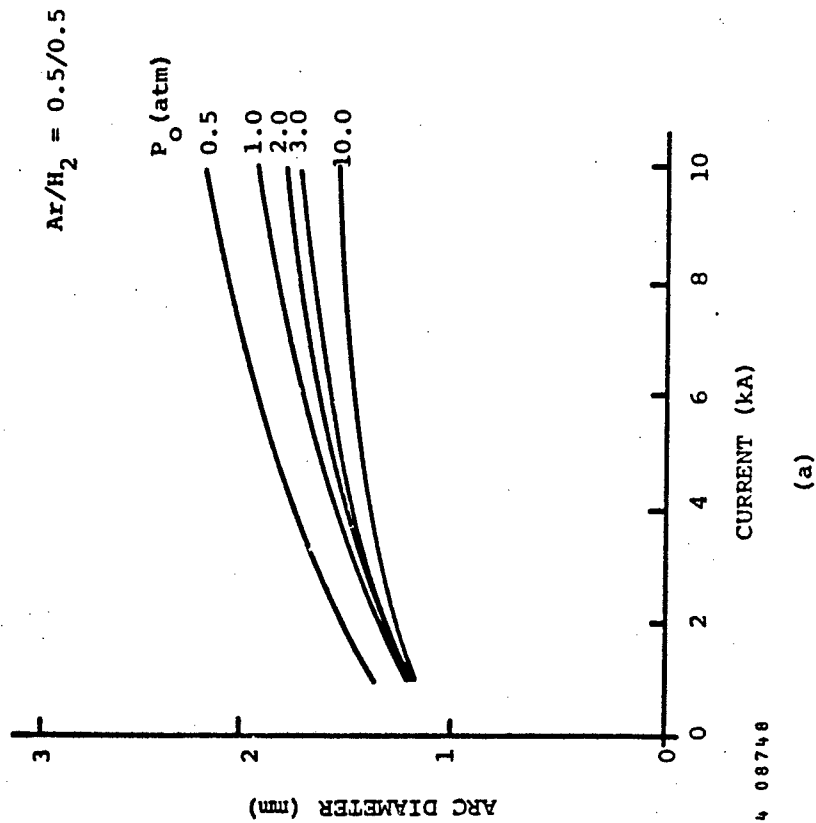
Figure VI-6   Simple Model Results for a Spark Column in an Ar/H$_2$:0.5/0.5 Gas Mixture as a Function of Total Current and Different Initial Pressures. (a) Arc diameter; (b) arc temperature.

84 08748

VI-18
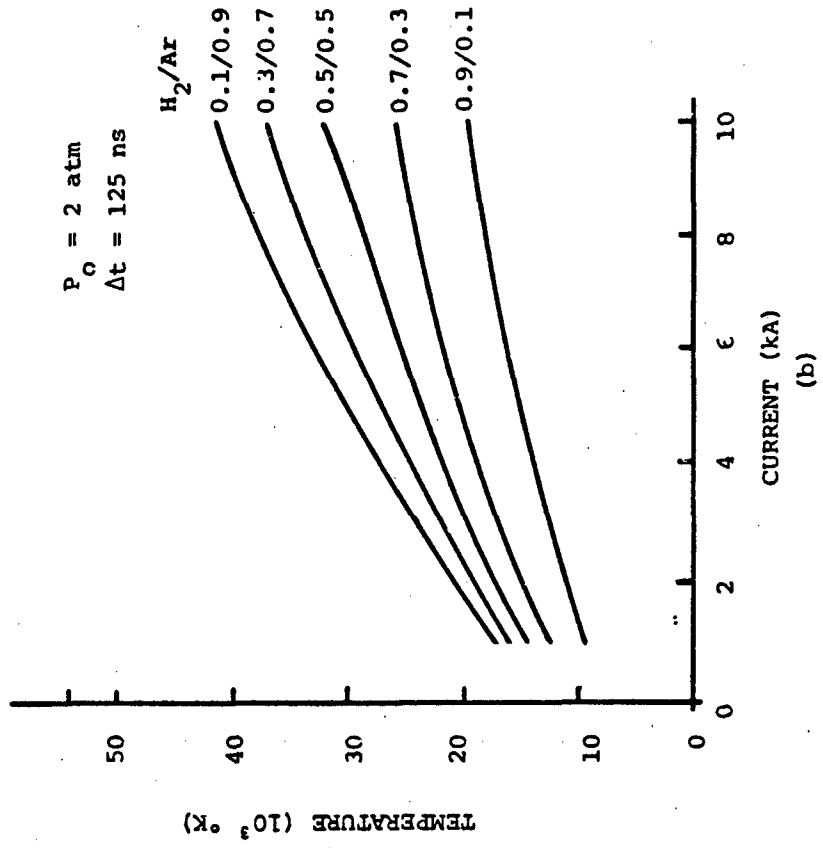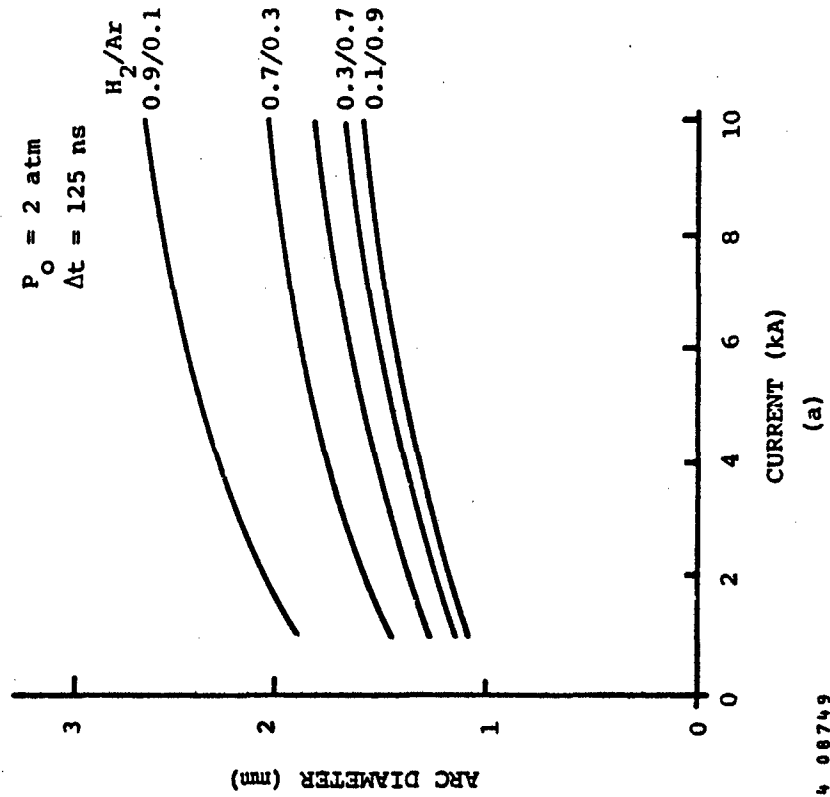
Figure VI-7 Simple Model Results for a Spark Column for an Initial Pressure of 2 atm in Different Ar/H₂ Gas Mixtures as a Function of Total Current. (a) Arc diameter; (b) arc temperature.

84 08749

References for Section VI

VI.1)   Naval Surface Weapons Center Contract No.   N60921-83-C-A057

VI.2)   P.J. Shayler and M.T.C. Fang, J. Phys. D. <u>10</u>, 1659 (1977)

VI.3)   G.H. Herzberg, <u>Molecular Spectra and Molecular Structure I. Spectra of Diatomic Molecules, 2nd Edition</u>, (New York: Van Nostrand), 1950.

VI.4)   N.M. Reddy, Aerononautical Quarterly <u>25</u>, 287 (1974)

VI.5)   C.E. Moore, <u>Atomic Energy Levels, Vol. I</u> (National Bureau of Standards NSRDS-NBS 35, Washington D.C.)   1971.

VI.6)   W.F. Hagen "Evaluation of the Iodine Laser", Max Planck Institut Fur Quantenoptik Report MPQ 52, Sept.   1981.

VI.7)   M. Mitchner and C.H. Kruger, <u>Partially Ionized Gases</u> (New York: Wiley-Interscience) 1973.

END

FILMED

12-84

DTIC